

Axonal spike initiation can be maintained with low axonal Na channel density, but temporal precision of spiking is lost

Elinor Lazarov, Melanie Dannemeyer, Barbara Feulner, Jörg Enderlein, Michael J. Gutnick, Fred Wolf, Andreas Neef

Abstract

In central neurons, action potentials (APs) originate in the axon initial segment (AIS) presumably due to its high concentration of voltage-dependent sodium (Nav) channels. In the AIS, Nav and their cytoskeletal anchoring proteins display a highly periodical nanoscale arrangement with unknown functional relevance. In mouse hippocampal neurons, we examined a mutation of the AIS-specific protein βIV -spectrin and assessed AP initiation locus, AIS molecular organization, and the precision of *in vivo*-like AP encoding. In mutants, Nav concentration was strongly reduced in AIS but not soma, while AIS nanoscale organization was preserved. Surprisingly, APs still originated in the axon, even if the axonal channel density was as low as in the somatic membrane. However, the timing of those APs was less precise, therefore the neuron's encoding bandwidth was substantially decreased. Therefore, the high Nav density in the AIS is not required for axonal AP initiation, it is crucial for AP timing precision.

Keywords: Axon initial segment, βIV -spectrin, onset rapidness, spike generation, dynamic gain, $\text{qv}^{3\text{J}}$ mutation

Introduction

In central neurons, action potentials (AP) are initiated in the axon initial segment (AIS), a specialized compartment in the proximal axon that extends tens of micrometers from the cell body. The heightened excitability of this region has been attributed to several factors: 1) a high density of voltage-dependent sodium channels (Nav) in the AIS (Fleidervish et al., 2010; Kole and Stuart, 2012; Lorincz and Nusser, 2010), 2) a shift of the voltage dependence of Nav activation in the AIS to less depolarized voltages (Colbert and Pan, 2002; Hu et al., 2009; Kole et al., 2008), and 3) electrotonic distance of the AIS from the electric load of the soma, which renders distal Na^+ -influx more efficient for *local* membrane depolarization (Baranauskas et al., 2013; Brette, 2013; Moore et al., 1983).

APs are the currency of information exchange between neurons in the brain. How precisely an AP sequence reflects the neuron's input can be quantified by repeatedly providing the same input (frozen noise) and assessing reproducibility of AP timing. High AP timing precision is closely related to the neuron's ability to represent a wide range of frequency components in the input, the bandwidth of encoding.

In pyramidal neurons, the bandwidth of encoding has been experimentally shown to be surprisingly wide, extending to frequencies above 200 Hz (Boucsein et al., 2009; Higgs and Spain, 2009; Ilin et al., 2013; Kondgen et al., 2008; Ostojic et al., 2015; Tchumatchenko et al., 2011; Testa-Silva et al., 2014). Different hypothesis have been proposed to explain the experimentally observed high encoding bandwidth. These include the overall distribution of electric load between dendrites soma and axon (Eyal et al., 2014; Ostojic et al., 2015), the electrotonic separation of the AIS initiation site from the soma (Brette, 2013), and the details AP dynamics at the initiation site (Ilin et al., 2013; Naundorf et al., 2005, 2006; Wei and Wolf, 2011). Critically testing these competing hypotheses and thus determining the biophysical and molecular basis of high encoding bandwidth requires manipulating these features with a high specificity that up to now remained elusive.

In the present study, we have sought to experimentally study the role of axonal sodium channels in AP initiation and information encoding in an experimental model system that

allows us to manipulate the properties of the AIS without disturbing other neuronal compartments. Our approach builds on recent progress on the molecular specializations of the AIS (Berghs et al., 2000; Ogawa et al., 2006; Rasband, 2010; Yang et al., 2004). Among the known mutations of AIS component proteins a group of β IV-spectrin mutations, causing quivering in mice, stands out as closely linked to AP precision. Auditory evoked brainstem potentials, which reflect the coherence of AP generation across a population of neurons, were deteriorated in various *qv* mutations (Parkinson et al., 2001).

β IV-spectrin and ankyrinG (AnkG) are key structural proteins that control the creation and maintenance of the AIS (Hedstrom et al., 2008; Jenkins and Bennett, 2001; Komada and Soriano, 2002; Yang et al., 2007; Zhou et al., 1998). Both proteins are exclusively found at the AIS and the nodes of Ranvier (Bennett and Baines, 2001). β IV-spectrin is part of a membrane undercoat formed by cytoskeletal proteins (Fig. 1A). Most importantly, β IV-spectrin tethers AnkG to the actin-spectrin network (Fig. 1B). AnkG, in turn, anchors voltage dependent potassium and sodium channels (Nav). Phosphorylation and dephosphorylation of different ion channel subtypes control their binding affinities to AnkG (Xu and Cooper, 2015). Thus, β IV-spectrin is a central player in the protein-protein interactions that maintain and regulate the composition of the AIS. We have used a mutation of this protein to change the number of ion channel in the AIS. The *qv*^{3J} mutated β IV-spectrin features a scrambled C-terminus due to a frame-shifting base insertion in the *Sptnb4* gene (Fig. 1C). We chose this mutation for two reasons: 1) mice with related quivering (*qv*) mutations of the β IV-spectrin gene show a reduced acuity of action potential timing in the auditory spiral ganglion neurons (Parkinson et al., 2001). 2) the *qv*^{3J} mutation is the most conservative of all *qv* mutations and causes a mild, progressive phenotype that reflects a gradual change in the morphology of the AIS and the nodes of Ranvier over the course of postnatal development (Parkinson et al., 2001; Yang et al., 2004, 2007).

Studies on molecular consequences of the *qv* β IV-spectrin mutations predate the discovery of the nanoscale regular organization of the AIS cytoskeleton, where actin rings line the circumference of the AIS every 190 nm (Xu et al., 2013). This distance is maintained by

several parallel, longitudinally running spectrin strands that contain β IV- but also β II-spectrin (Zhong et al., n.d.). The functional relevance of a regular organization on the scale of 200 nanometer is unclear. Here, we have used STORM imaging to determine whether the qv^{3J} mutation is associated with a modification of this regularity.

In the present study we used patch clamp recordings, immunocytochemistry and super-resolution microscopy to describe the functional consequences of the changes in AIS protein composition associated with the qv^{3J} mutant. We find that, although β IV-spectrin is lost in mutants already after one week, densities of AnkG and Nav remain at their initial levels for several days, eventually dropping off to below detection threshold. By contrast, densities of AnkG and axonal Nav steadily increase in controls. Because Nav density in the soma is not altered in the mutant and the regularity of the AIS cytoskeleton is preserved, the qv^{3J} mutant is an excellent experimental system to characterize the effects of reducing the Nav density specifically in the AIS. This enabled us for the first time to experimentally scrutinize the view that high AIS channel density is “an absolute requirement” for an axonal locus of AP initiation (Kole and Stuart, 2012). To our surprise, we found that even when the axonal Nav density was drastically reduced, APs still initiated in the AIS and not in the soma. The reduction of axonal Nav density, however, functionally impaired the quality of AP encoding even though the APs still originate in the AIS. APs were far less precisely timed when the Nav density in the AIS was low. Biophysically realistic computational models show that both observations, the maintained axonal origin of APs and their deteriorated timing, can be largely accounted for by a reduction of axonal densities of Nav and Kv. We conclude that the main consequence and benefit of high axonal channel density is an improved encoding of information by precisely locking APs to transient changes in the input.

Results

Mice carrying the qv^{3J} mutation show progressive neurological dysfunctions. We therefore expected that early in development the functional deficits on the cellular level would be

mild and aggravate only with maturation. Furthermore, the exclusively axonal localization of the mutated spectrin led us hypothesize that the structural deficits caused by the mutation might also be restricted to the AIS. This would allow us to study the consequences of AIS defects onto AP initiation and spike time precision.

Information encoding in qv^{3J} mutants

Cortical neurons often encode information as elements of a large population of neurons. The information is encoded in the rate of APs produced by the population and received by downstream neurons. How precisely the information is encoded can be studied in the time domain or the frequency domain. In the time domain, the precise timing of spikes can be assessed by comparing responses to identical trials of fluctuating input, so called frozen noise. In the frequency domain, the encoding can be characterized by a dynamic gain. Here we use both approaches.

In whole-cell current clamp mature neurons from mice homozygous for qv^{3J} (mutants) and control littermates were stimulated by injection of fluctuating currents with a correlation time of 35 ms, a value close to the typical membrane time constant (Fig. S1A, Methods). The standard deviation was adjusted to obtain a firing rate of approximately 2 Hz (control $\nu=1.95$ Hz (0.60) , $n=11$; qv^{3J} $\nu=2.03$ Hz (0.86), $n=16$). AP shapes and firing frequency showed no sign of adaptation throughout the 50s long stimulation episodes. Firing was highly irregular, the local variation of inter-spike intervals (Shinomoto et al., 2009) was on average $lv=1.05$ (SD 0.09) for controls and $lv=1.06$ (SD 0.08) for qv^{3J} mutants. Fast spiking neurons, putative interneurons, had been excluded from analysis (Fig. S1E).

To quantify the bandwidth of frequencies that the cells can encode in their AP firing patterns, we followed the approach of Higgs and Spain (Higgs and Spain, 2009) to calculate the dynamic gain. This function reveals, how well the neuron can lock its APs to current fluctuations at different input frequencies. It expresses the susceptibility of the neurons in Hz/nA. The overall shape of the dynamic gain is similar for both genotypes, the dynamic gain curves peak around input frequencies of 30 Hz and fall for higher frequencies (Fig. 1F,G). However, the gains of qv^{3J} mutants drop at lower frequencies than the control

curves. This is evident from the non-overlapping bootstrap confidence intervals for the two populations. To further characterize the difference, we compared the frequency at which the gain of individual cells drops to 60% of the peak value (Fig. 1F). This cut-off frequency was 36% smaller in qv^{3J} mutants (Fig. 1H).

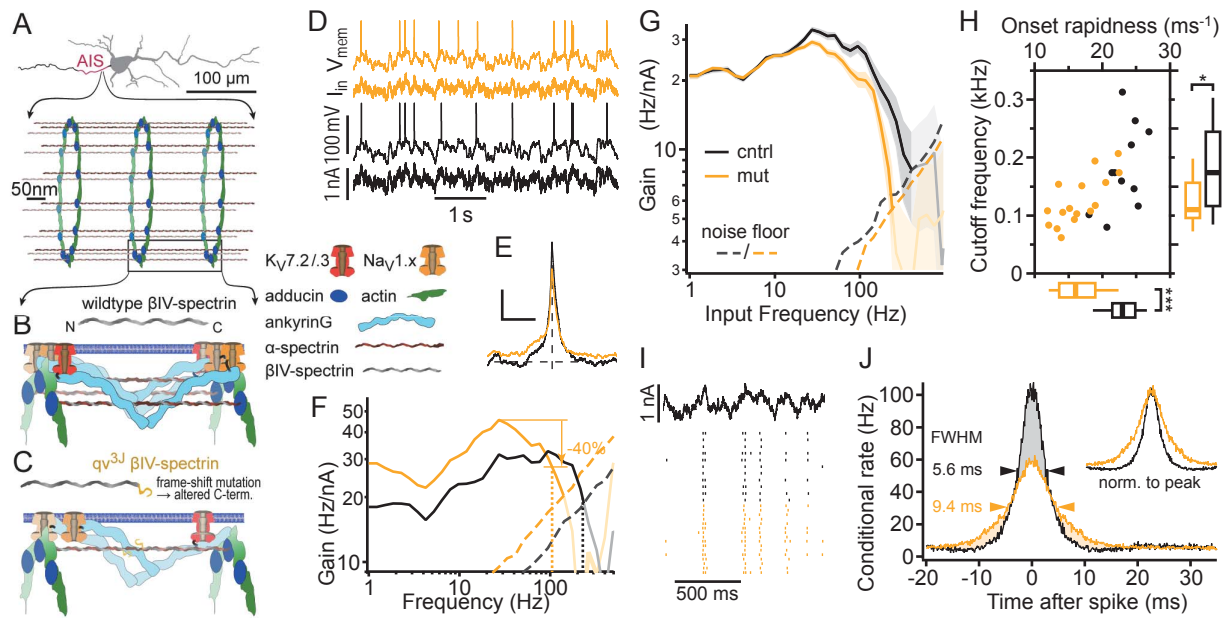


Figure 1: Reduced precision of AP timing and slower AP onset in qv^{3J} mutants. A The axon cytoskeleton in the AIS is highly regular. Tetramers of α - and β -spectrin serve as 190 nm long spacers between rings of actin. B Na_V - and K_V -channels are anchored to AnkyrinG, which binds to β IV-spectrin and the lipid membrane. C The qv^{3J} mutation affects the very C-terminal portion of β IV-spectrin. We hypothesized that this might lead to a reduction in the number of intact tetramers and hence a reduction of AnkyrinG and ion channels. D Fluctuating input current (I_{in} , see Methods) and the resulting membrane voltage (V_{mem}) of one control neuron (black) and one qv^{3J} mutant neuron (orange). E Spike triggered average current of the two neurons from D, scale bars are 0.1 nA and 200 ms. F Dynamic gain for the two neurons (continuous lines) was considered significant up to the intersection with the noise floor (dashed lines). For calculations of gain and noise-floor see Methods. The cut-off frequency (dotted lines) for each gain curve was set as the point where the gain falls below 60% of its peak value. G Average dynamic gain of mature (>21 DIV) neurons from qv^{3J} mutant mice and control littermates (wild type and heterozygous). Control: n=11 cells; median age 31 DIV; 5,223 spikes; mutant: n=16; median age 29 DIV; 7,909 spikes). The frequency response function of mutant neurons (orange) drops at lower frequency compared with control (black) neurons (average with 95% confidence interval, see methods). Gain curves were considered significant until the intersection with the noise-floor (dashed). H Cut-off frequency plotted against AP onset rapidness (see figure 2 B and D) for mutant and control cells. Box plots (median, quartiles and 10/90 percentiles) characterize the marginal distributions. The cut-off frequency was significantly lower ($p = 0.0182$) in mutants (125.4 ± 10.6 Hz; mean \pm SEM) than in controls (181.2 ± 21.8 Hz). The AP onset rapidness was significantly smaller in mutants (16.5 ± 0.9 ms $^{-1}$) than in controls (23.1 ± 0.8 ms $^{-1}$); $p < 0.0001$, while no difference was found for the average membrane time constant (τ_m control: 29.1 ± 2.4 ms; τ_m mutant: 29.1 ± 3.5 ms) or peak rate of rise (control 316 ± 23 V/s; mutant 296 ± 20 V/s), neither is shown here. * $p < 0.05$, *** $p < 0.001$. I In response to frozen noise (top, stochastic stimulus 1,

shown is the average fluctuation amplitude used across all 27 cells), 16 mutant and 11 control neurons fire APs locked to the stimulus. Shown is a 2 s long interval with a slightly higher than average activity. J Quantifying the precision of AP firing with the average conditional firing rate of pairs of neurons (see methods), the qv^{3J} neurons show a broader peak, indicative of a reduced precision.

A more direct assessment of AP timing precision is conditional firing rate, computed for two AP sequences fired in response to the same fluctuating input (Fig. 1I). As we used the same five stochastic stimuli for every neuron, we can characterize how precisely the population of neurons locks to the stimulus by computing the conditional firing rate for the two AP trains that a pair of neurons fired in response to the same input waveform. For threshold neuron models the conditional firing rate under frozen noise and the dynamic gain function are directly related (Tchumatchenko and Wolf, 2011). A tight locking between stimulus and AP initiation leads to little temporal jitter between the AP times of different neurons under the same stimulus (Fig. 1I) and hence to a high and narrow conditional firing rate (Fig. 1J). Averaging across all neuron pairs, we found that for the qv^{3J} mutation, the average conditional firing rate has a smaller peak value and is broader: 9.4 ms full width at half maximum compared to 5.6 ms for the control neurons. Just as the reduced bandwidth of the dynamic gain, the broadening of the conditional firing rate reflects a less precise alignment between APs and the stimulus in the case of the qv^{3J} mutant.

The initial but not the somatic phase of APs is affected by qv^{3J}

In order to identify the functional basis of the reduced AP timing precision, we studied the AP waveform in neurons from qv^{3J} and control littermates throughout development, starting in the second week, just after the onset of AP firing, until the sixth week in vitro, using whole-cell patch clamp. During the first two weeks of this period, the membrane capacitance and conductance, assessed by short subthreshold current pulses, increased by about 50% and 100% respectively (Fig. 2A). This reflects a growth of the somato-dendritic compartment and occurred in both genotypes. During the earliest phase of an AP, when the AIS is more depolarized than the soma, the somato-dendritic membrane is charged by current flow from the AIS. This lateral current underlies the first phase of depolarization

in the somatic AP waveform (Fig. 2B and S2). We elicited APs by 100 ms current pulses, starting from a membrane voltage of -76 mV. The first AP evoked within a few milliseconds after current onset is analyzed as shown in the phase plan plot in Fig. 2B and explained in the methods. The early phase, associated with AP initiation, is characterized by the threshold voltage and the steepness of the phase plot at the threshold, i.e. the onset rapidness (Fig. 2C and D). The second part of the AP upstroke is characterized by the peak rate of voltage rise, and the peak voltage (Fig. 2E and F).

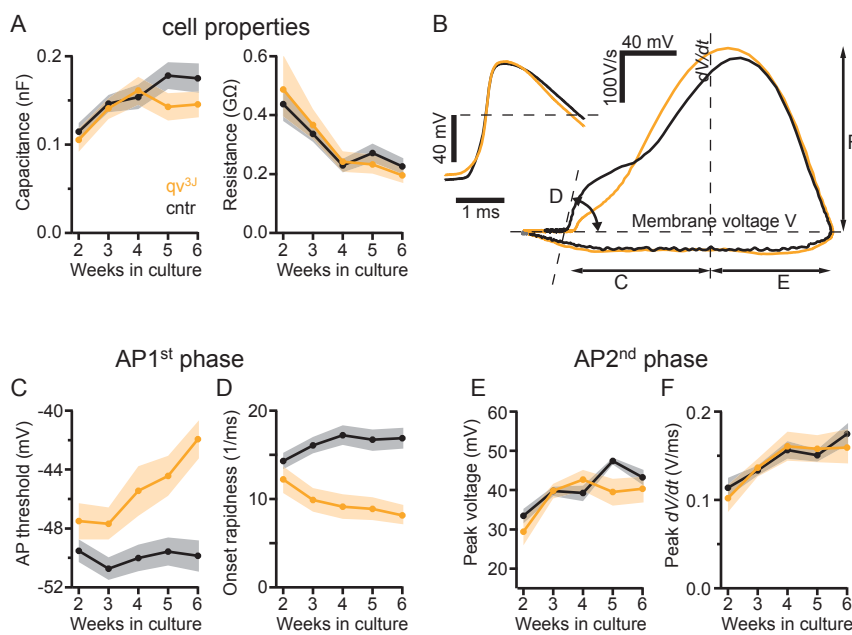


Figure 2: APs of qv^{3J} mutants show depolarized threshold voltage and slower onset rapidness compared to control. A. The qv^{3J} mutation has no effect on the cell membrane properties. Cell capacitance and resistance are similar in mutant and control littermates at different time points in culture development. B. Representative phase plots (dV/dt vs V) from mature (> 21 DIV) mutant (orange) and control (black) neurons, exemplifying the effect of

the qv^{3J} mutation on the first, but not on the second phase of the AP. Arrows and letters indicate the quantifications of AP waveform used in C through F. C-D. The quantifiers of the early AP phase, threshold and onset rapidness, increasingly diverged between qv^{3J} and control during development. The difference between mutants and controls was significant already after the second week *in vitro*. E-F. The second phase of the AP was unaffected by the mutation. The peak voltage and peak rate of rise have similar values in both mutants and controls. A and C – F Number of cells: $n_{mutant} = 36, 44, 36, 47, 43$; $n_{control} = 70, 96, 78, 41, 50$. Shaded area represents 95% confidence interval.

We observed no effect of qv^{3J} on passive cellular properties (Fig. 2A) and also no effect on those features of the AP waveform that are dominated by ion channels in the soma (Fig. 2E and F). The 95% confidence intervals of those properties in mutants and control overlap at almost all developmental stages. In contrast, for AP properties that are dominated by axonal ion channels the mutation showed a clear effect. In qv^{3J} neurons AP initiation

requires a more depolarized somatic potential (Fig. 2C) and it progresses more slowly (Fig. 2D). The differences were small in the second week in cultures but during the next 4 weeks they increased until the onset rapidness in mutants was only 48% of control (17 ± 1 vs 8 ± 1 ms⁻¹) and the threshold potential differed by 8 mV (-50 ± 1 vs 42 ± 1). The fact that the mutation of a protein expressed only in the AIS has effects that appear to be limited to AP initiation, which occurs in the AIS, may suggest unchanged development of somato-dendritic compartments. However, the nature of whole-cell patch clamp measurement does not directly provide a spatial resolution that would further support this interpretation or more quantitative statements on the differences of axonal currents. To further investigate the effects of the qv^{3J} mutation with spatial resolution, we turned to immunocytochemistry.

β IV-spectrin is lost early on, Nav channels cannot be stabilized or recruited

In the AIS of control neurons we observed, at all studied time points, strong signals from antibodies against AnkG, β IV-spectrin and Nav (pan-Nav). Example images for the fourth week are shown in Figs. 3A and S3A. To quantify the spatial distribution of the immunosignal, we obtained the fluorescence intensity profile along the axon (Figs. 3B,C; S3B,C), starting at the soma or, in the case of axons branching off a dendrite, starting at the last branching point. As expected from the electrophysiology results, the Nav signal in the AIS increases over time, consistent with (Yang et al., 2007). The fluorescence intensity of AnkG antibodies increased as well, similar to very recent observations (Yoshimura et al., 2017). When we turned to neurons from littermates homozygous for qv^{3J} , we first asked whether β IV-spectrin is still present at the AIS. Only at the earliest time point studied, at day in vitro 7, shortly after AIS assembly, we could detect a β IV-spectrin signal (Fig. S3D). Even then, the fluorescence intensity was much weaker compared to the control group (mean \pm std of intensity along the first 30 μ m of the AIS, 4.9 ± 1.2 [AU] in the mutants, n=4 cells; 105.6 ± 58.8 [AU] in controls, n=4 cells).

In contrast to the controls, qv^{3J} neurons failed to accumulate AnkG or Nav in the AIS during development (Fig. 3B, orange profiles). Therefore the density of Nav at the AIS is lower

in the mutant. A similar observation had been made for voltage gated potassium channels (Devaux, 2010). Given the low fluorescence signals in qv^{3J} , it was not always possible to identify the axon as the one neurite that featured a stronger immunostaining in the proximal part. The intensity profiles in Fig. 3 and Fig. S3 represent the subset of qv^{3J} neurons where AIS identification succeeded. When we combined pan-Nav and AnkG staining in a separate group of experiments, covering a shorter developmental period, we found that AnkG labelling allowed AIS identification even in cases where none of the neurites showed an outstanding Nav signal. We attribute this reliability of AnkG staining to the fact that, unlike pan-Nav, AnkG antibodies did not label soma and dendrites. This allowed us to identify the axon even in part of the cells, where the Nav label did not allow a clear AIS identification. The fraction of AnkG-positive but Nav-negative AIS grew over time (Fig. 3D) from 8% at 10 days in vitro (DIV) to 66% at 19 DIV.

Remarkably, despite the strong reduction of Nav immuno-labelling at the AIS, the density in the soma appeared unaffected by the mutation (Fig. 3D). Therefore, electrophysiological assessment (Fig. 2A,B, F and G) and immunostaining both indicate that the structural and functional consequences of the qv^{3J} mutation are restricted to the AIS, while the structural and electrical maturation of the somato-dendritic compartment is preserved. The spatially restricted effects of the qv^{3J} mutation point to an axonal cause for the observed reduction in AP time precision and the ability to track high frequency components in the input.

The observed early loss of β IV-spectrin suggests that the frame shift mutation towards the C-terminus removed an important interaction site that supports the retention of β IV-spectrin at the AIS. The subsequent loss of AnkG and Nav could be simply a consequence of the disappearance of β IV-spectrin, however, it is unclear how the remaining AnkG and Nav proteins are stabilized at the AIS, when β IV-spectrin is already lost. Furthermore, the complete loss of this key structural protein prompts the question, whether the nanostructure, that is thought to rely on spectrin tetramers, is also destroyed in qv^{3J} .

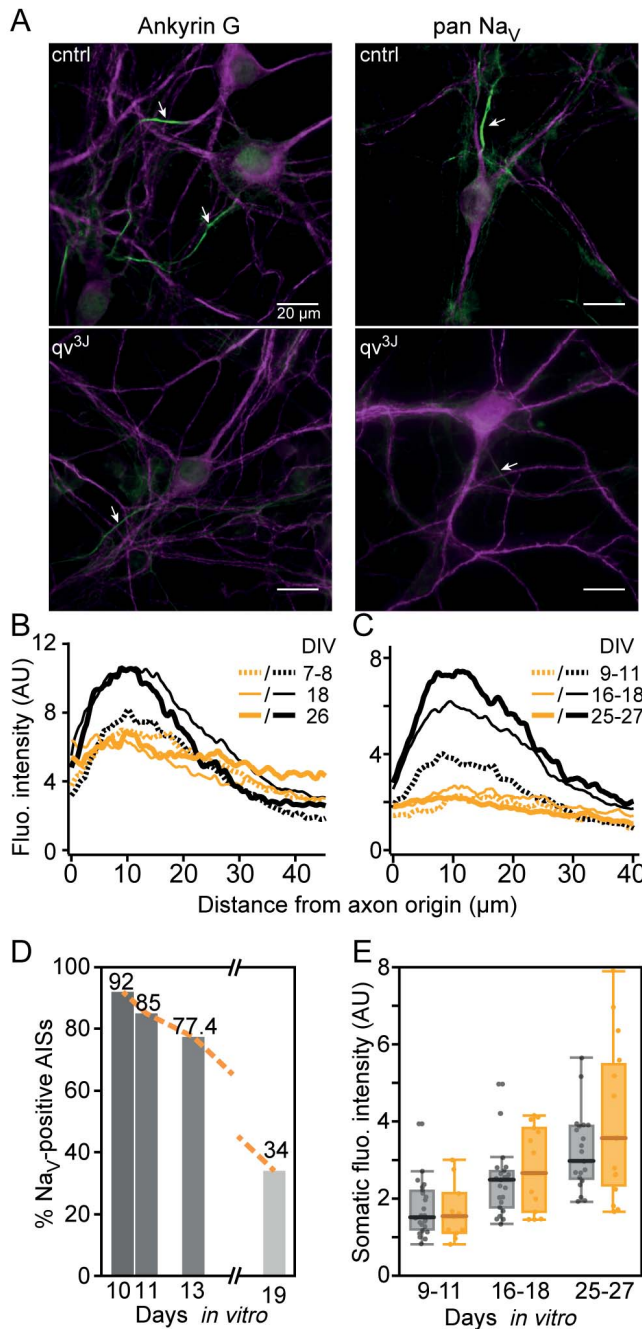


Figure 3 Lower densities of Nav channels and AnkG in the AIS of mature qv^{3J} mutant neurons.

A. Hippocampal neurons, 26 days in culture, from mutant and control animals were labeled with antibodies against MAP2 (red) and either Nav_v channels (pan-Nav_v) or AnkG (green). Scale bars: 20 μm. B. Profiles of AnkG immunosignal along the AIS, starting where it branches off the soma or a dendrite. Data from mutant are shown in orange, control in black at three developmental stages: 7-8 DIV, 18 DIV, 26 DIV ($n_{\text{mutant}} = 25, 17, 14$; $n_{\text{control}} = 26, 32, 25$). C. As in B, but for pan-Nav_v immunolabelling: 9-11 DIV, 16-18 DIV, 25-27 DIV ($n_{\text{mutant}} = 13, 16, 19$; $n_{\text{control}} = 38, 83, 32$). In most mature mutant cells (>21 DIV) we could not identify an AIS based on its stronger pan-Nav_v staining. The line profile shown here was obtained from the subset of neurons that still demonstrated an evident staining. To reduce cluttering, only the averages are shown in B and C, confidence intervals are shown in figure S3. Note that AnkG and Nav_v channels fluorescence intensity at the AIS of mutant cells remains low throughout maturation (orange curves), but increase in control cells (gray curves). D. In a separate data set, covering a smaller developmental period, cultures were double stained for AnkG and pan-Nav. Here axons could be identified by AnkG label even when no neurite showed enhanced pan-Nav staining. Among the AnkG-positive axons, the fraction pan-Nav positive AIS' decreased during development (N = 12, 13, 84, 35.). E. Average somatic pan-Nav fluorescence intensity is similar in control and qv^{3J} mutant cells during development, suggesting it is unaffected by the

mutation. $n_{\text{mutant}} = 11, 15, 16$; $n_{\text{control}} = 24, 23, 21$. AU, arbitrary units of camera signal, obtained under standardized conditions.

AnkG and Nav channels retain their regular organization in qv^{3J} AIS

On the level of cellular physiology and micrometer scale immuno-localization, our data and modeling analysis suggest that the qv^{3J} mutation entails a loss of axonal proteins and that the loss of axonal channels underlies functional impairments. We now wanted to probe whether the AIS nanostructure is affected by the mutation. Does the loss of β IV-spectrin and AnkG perturb axo-skeleton periodicity? Currently, it is not known, whether the regular nano-structure of the AIS cytoskeleton crucially depends on β IV-spectrin. It is also not clear, whether its regularity has any effect on AIS function.

We investigated the nanoscopic organization of AIS proteins using dSTORM (direct stochastic optical reconstruction microscopy), with Alexa 647 labelled antibodies. As reported (van de Linde et al., 2011), the individual fluorophores localizations had a precision of 10-20 nm. In accordance with previous studies (Leterrier et al., 2015; Xu et al., 2013; Zhong et al., n.d.) we found that AnkG and Nav channels are periodically spaced in the AIS, shown by a pronounced peak in the power spectrum of localization profiles at a spatial frequency of 1/190 nm (Fig. 4). Our data show that both AnkG and Nav channels retain their periodic distribution in the AIS despite the complete loss of β IV-spectrin in the mutant. In fact, the periodicity of AnkG seemed more pronounced compared to control cells, possibly due to the reduced protein density. At 19 DIV, when the majority of mutant AIS do not display a discernible Nav labelling, the spectral power at 1/190 nm of the Nav label is reduced in the mutant. This break-down of regularity is likely due to the sparsity of Nav. Lower spatial frequencies are over-represented as it would be expected when individual spots contain no Nav-label at all.

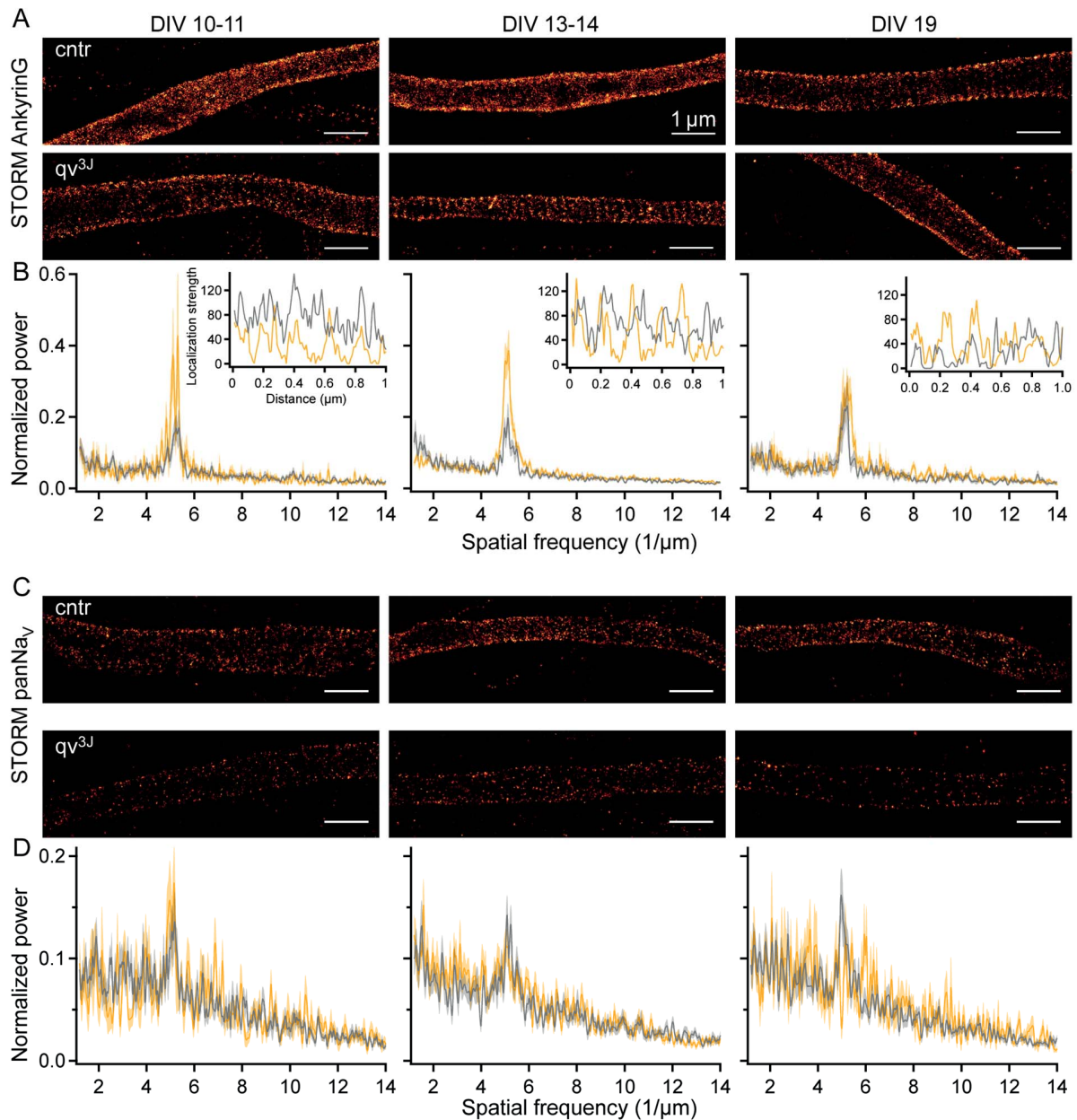


Figure 4: The structural organization of AnkG and Nav channels appears unaffected by the *qv^{3J}* mutation. A. dSTORM images of AISs of control (top) and mutant (bottom) neurons, labeled with antibodies against AnkG (N-terminus) at DIV 10-11, 13-14 and 19. Scale bar: 1 μ m. B. Power spectra analysis of AnkG immunofluorescence profile along the AIS of control (n= 17, 28, 14) and mutant (n= 9, 53, 22) cells, demonstrating periodic pattern in both populations at the 3 time points, with periodic length of about 190nm. Examples of individual immunofluorescence profiles along 1 μ m segments are shown in the insets. C. Same as A, with antibodies against Nav channels. D. Power spectra analysis of the pan-Nav immunofluorescence profile along the AIS of control (N = 20, 33, 33) and mutant (N = 10, 29, 12) cells, demonstrating periodic pattern in control population at all 3 time points, with periodic length of about 190nm. In *qv^{3J}*, periodicity at 190nm is reduced and peaks appear at lower spatial frequencies, as less localizations occur and the grid is not fully decorated. Errors represent SEM.

Modeling predicts that APs initiate in the axon despite low axonal Na_V density

Our experimental results strongly suggest, that the qv^{3J} mutation of βIV -spectrin leads to a reduction of sodium channels in the AIS, but not the soma and that the remaining Na_V -channels are still clustered, similar to channels in the wild-type, albeit with a much lower density. We next tested, whether the reduction of axonal ion channel density alone is sufficient to reproduce the observed changes in AP initiation and AP timing precision in a biophysical neuron model. To this end we used a previously published multi-compartment model of AP initiation in pyramidal neurons (Hallermann et al., 2012) and tested it with current injections equivalent to the step currents and fluctuating currents used in the electrophysiological experiments. As many hours of simulated time were required to obtain dynamic gain curves for different conditions, we compacted the models morphology and thereby considerably sped up simulations (see Methods). The model features one type of Na_V in the soma and proximal axon and a second type of Na_V in the more distal AIS. As earlier results (Devaux, 2010) suggest that also K_V -channel recruitment is affected by the qv^{3J} mutation, we next reduced all ion channel densities in the axon and studied the consequences in AP waveform and dynamic gain (Fig. 5A,B). Indeed, the effects of the density reduction mirrored closely the electrophysiological findings. The early phase of the somatic AP waveform was strongly reduced in size, while the second, somatic phase was very weakly affected. AP threshold became more depolarized and onset rapidness was reduced (Fig. 5B, as was the bandwidth of the dynamic gain (Fig. 5A). It is worth noting, that we had not chosen or designed the model for these effects, but rather used an existing model for AP initiation.

Unlike the whole cell patch-clamp experiments, the simulations allow a direct comparison of voltages from different cellular locations, so the axonal origin of AP initiation can be tested directly. Plotting the axonal membrane voltage against the somatic voltage during AP onset confirmed that the loss of a biphasic AP phaseplot in the soma indeed indicates a somatic initiation (Figs. 5B, C). However, this shift of initiation from the AIS into the soma occurred only for very strong reduction of AIS channel densities. Even when the

axonal channel densities were below the somatic densities, at 5% of the original density, APs were still initiated in the axon similar to observations in early computational studies on the site of AP initiation (Moore et al., 1983). Next, we set out to test whether this simulation result could be confirmed in patch-clamp experiments.

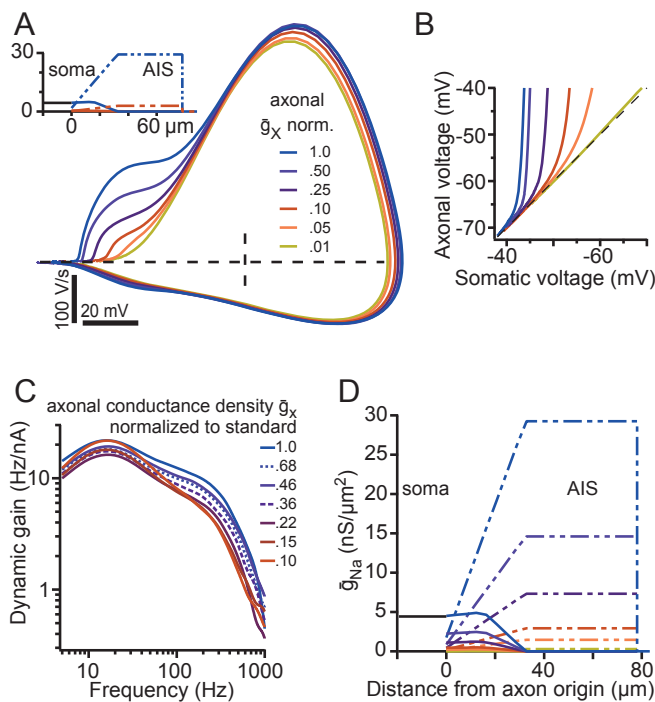


Figure 5: Reducing axonal channel densities suffices to replicate effects of qv^{3J} mutation in a model A. We used a multi-compartment model based on a previously published model of AP initiation in pyramidal neurons (Hallermann et al., 2012) to test whether reduction of AIS channel densities suffices to replicate the experimental findings. The inset illustrates the conductance densities (in $nS/\mu m^2$) of the two types of Na_V -channels in the model. Blue corresponds to the standard densities, red to a 90% reduction. In the latter case the somatic conductance density is higher than the axonal one. As the axonal channel densities were reduced, the simulated somatic AP waveform showed the changes we observed in mature qv^{3J} neurons. Threshold was shifted and the initial lateral current into the soma was less pronounced, in particular the initial slope in the phase plot decreased

from $29 ms^{-1}$ to $4.6 ms^{-1}$. In contrast, the second phase of the AP waveform remained largely unchanged. Biphasic phase plots were obtained for density reduction as severe as 95%. Only for 99% reduction the phase plot appeared monophasic. B. Axonal depolarization ($50 \mu m$ from soma) preceded somatic depolarization during AP initiation for all channel densities that resulted in biphasic phase plots. Only for a 99% reduction of channel densities no sign of axonal initiation could be detected. C The model neurons were driven with fluctuating current with the same correlation time as in the experiments (35 ms) and at the same firing rate (2 Hz). Dynamic gain curves showed a reduced bandwidth, when the channel densities in the axonal compartment were reduced to 1/10 in six exponentially spaced steps. D. The conductance densities for the two different Na^+ channel types in the model. All other conductances were also scaled down proportionally but are omitted here for clarity. Color code in A – D is identical, steps are identical in A, B and D.

Combined patch clamp and immunostaining confirms model prediction

On the one hand, the model's prediction of *axonal* AP initiation even under drastic reduction in axonal ion channel densities is surprising. It contradicts the consensus of a high ratio of axonal to somatic Na_V channel densities being crucial for axonal excitability. On the other hand, the prediction is in line with our electrophysiological recordings on

mature qv^{3J} . Biphasic AP waveforms indicate that axonal initiation occurs in qv^{3J} mutants even at a late developmental stage (Fig. S2, DIV 25 and DIV 30) when axonal Nav immuno-labelling becomes indistinguishable from dendritic or somatic labelling (Fig. 3D). Because electrophysiology and immuno-labelling had been performed on separate preparations, we next set out to apply both techniques in the same sample to test more strictly, whether AP initiation can occur in axons with Nav densities far below control levels.

We combined the AnkG / pan- Nav double-labeling that allows for AIS identification late in development (Fig. 3D) with electrophysiology in the very same neurons. We recorded APs from qv^{3J} mutant cells, ages 14 to 28 DIV and filled them with an Alexa dye through the patch-pipette. Immediately afterwards, the cultures were fixed and labeled with antibodies against AnkG and Nav channels, which allowed us to identify the AIS in 7 out of the 11 neurons (Fig. 6 & S4, see supplemental video). In most of the neurons Nav channel fluorescence intensity at the AIS was very weak and hard to distinguish from background levels. While some of those neurons indeed lost the biphasic AP rise (Fig. 6C), other neurons with similarly weak Nav channel staining had biphasic APs (Fig. 6A,B). This within-cell comparison of labelling and AP shape clearly confirmed that APs can still initiate at the axon even when Nav channel density is lower than the somatic density (Fig. 6A,B).

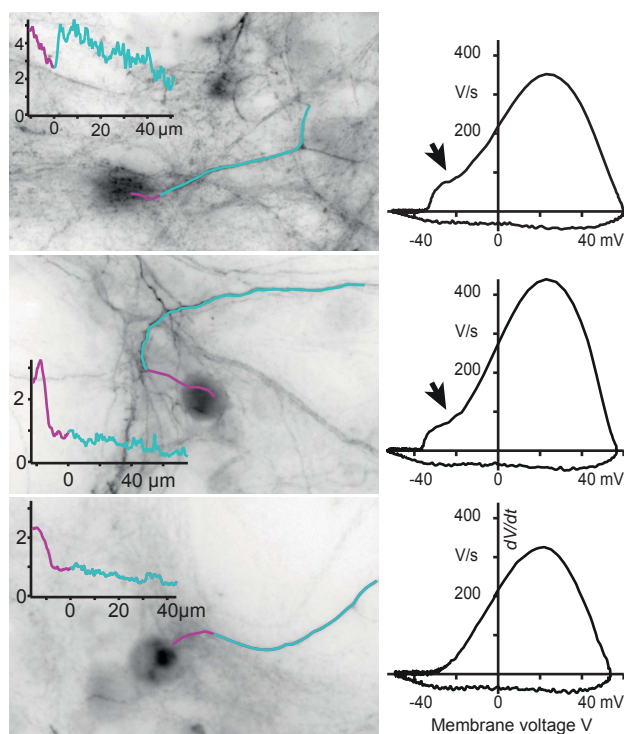


Figure 6: Immunolabeling and phase plot analysis of homozygous *qv3J* mature neurons (24-28 DIV). A-B. The biphasic phase plots demonstrate that APs were still initiated in the soma even when fluorescence intensity profiles indicate that the axonal Nav channel density was either slightly larger than in the soma (A: 1.5 times higher) or even lower than in the soma (B). C. In this neurons, APs appeared to initiate in the soma as the phase plot shows no sign of any lateral current into the soma (compare figure 5B 99% reduction). The immunostaining in the same neuron reveals an axonal pan-Nav signal that is much lower than in the soma. The full data set comprising more neurons is shown in Fig. S4. Here, images were rotated for display purposes. A movie detailing the 3 fluorescence images used to identify the AIS and obtain the profile is in the supplemental data.

β II-spectrin is present in the AIS, preserving cytoskeleton nano-structure in *qv^{3J}*

The previous results draw a consistent picture of the functional effects of the *qv^{3J}* mutation and the underlying molecular changes. The structural finding however, i.e. the presence and regular arrangement of AnkG and Nav channels, weeks after β IV-spectrin had dropped under the detection limit, was surprising to us. In light of the crucial role that β IV-spectrin plays for the localization of AnkG and Nav channels to the AIS (Komada and Soriano, 2002; Lacas-Gervais et al., 2004; Uemoto et al., 2007; Yang et al., 2004), one might have expected a disintegration of the regular arrangement. Based on the observations by Zhong and colleagues (2014), we speculated that a β II-spectrin could still be present in the mature AIS, thereby providing binding sites for AnkG. Indeed, antibodies against β II-spectrin labeled the AIS, as defined by the presence of AnkG, of neurons from mutant and control animals at all developmental stages tested. While the fluorescence intensity of β II-spectrin decreased by \sim 40% with development, it was still pronounced in mature neurons (> 20 DIV) (Fig. 7A,B). The intensity of β II-spectrin label in the AIS did not differ between *qv^{3J}*

mutants and control, indicating that β II-spectrin is not upregulated in the mutant to compensate for the complete loss of β IV-spectrin. In addition, β II-spectrin (labeled close to its C-terminal) demonstrated a highly regular spacing of 190 nm (Fig. 7C,D), in agreement with (Zhong et al., n.d.). Together these findings suggest that β II-spectrin constitutes part of the periodic actin-spectrin cytoskeleton of the mature AIS, to which AnkG and Na_v channels bind. We did not detect an adverse effect on the remaining cytoskeleton caused by the loss of β IV-spectrin in the qv^{3J} mutant. Apparently, the primary consequence is a reduction in the density of AnkG and the associated voltage gated channels, rather than a loss of cytoskeleton regularity.

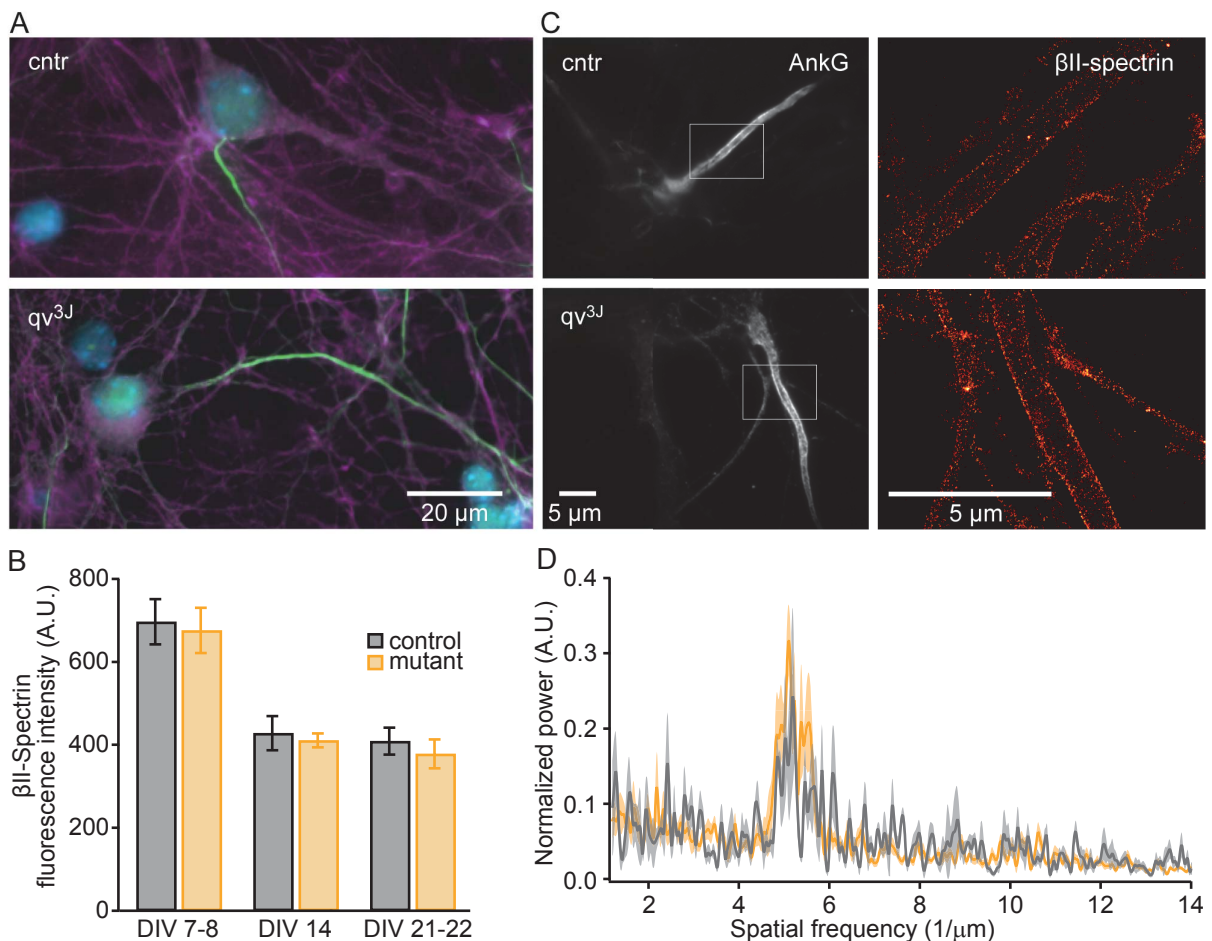


Figure 7: β II-spectrin is expressed at similar levels in the AIS of mutant and control cells and is part of the periodic cytoskeleton. A A culture of 8 DIV control (top) and qv^{3J} mutant (bottom) neurons double labeled with antibodies against β II-spectrin (red) and AnkG (green) (C-terminal). Nuclei were stained by DAPI (blue). B. β II-spectrin expression in control and qv^{3J} mutant neurons at three maturation stages.

The graph shows the mean fluorescence intensities in the AIS, within 50.0 μm from the soma or first branching point. Mutant and control cells showed similar βII -spectrin fluorescence intensities. βII -spectrin expression was reduced with development and shows no rescue for βIV -spectrin deficiency. Number of cells: $n_{\text{control}} = 36, 22, 27$; $n_{\text{mutant}} = 32, 11, 22$. Errors represent SEM. AU, arbitrary units. C. Antibodies against AnkG (C-terminus) were used to identify the AIS (gray) in control (top) and mutant (bottom) cells (DIV 13) and a region of interest was chosen for βII -spectrin dSTORM imaging (red). D. Power spectrum of βII -spectrin immunofluorescence profiles along the AIS of mutant (N=14) and control cells (N = 25) shows periodic organization in both populations, with periodic length of about 190 nm. βII -spectrin structural organization appears unaffected by the qv^{3J} mutation. Errors represent SEM.

Discussion

The qv^{3J} mutation in βIV -spectrin leads to a developmental loss of Nav channels selectively in the AIS while leaving the somato-dendritic compartment intact. This localized effect allowed us to pinpoint how channel density in the AIS relates to AP generation and precision. The results of electrophysiology, immunocytochemistry and multi-compartment models are consistent and demonstrate clearly that 1. Precise AP timing requires a high channel density in the axon, while 2. APs initiate in the axon even after dramatic reduction of axonal channel densities.

The control neurons in our study feature an AP waveform and encoding bandwidth that is qualitatively and quantitatively comparable to studies of pyramidal neurons in cortical layer 2/3 or layer 5 (Ilin et al., 2013; Kondgen et al., 2008; Tchumatchenko et al., 2011). This suggests that also our results on the relation between AIS channel density, AP initiation site and timing precision will generalize to neurons in-situ. In this context, it is interesting to note, that the neurons in our culture do not display myelination, as there are no oligodendrocytes present. On the one hand, the lack of myelination does not affect the formation of the AIS (Yang et al., 2007) and hence the molecular composition of the AIS in our preparation can be considered representative independent of myelin. On the other hand, the dynamical electrical properties of the AIS do change when myelin covers the axon at the distal end of the AIS. The reduction of membrane capacitance leads to a reduction of the capacitive load that the distal AIS experiences during AP initiation. In

consequence, the increased ratio of current to capacitive load would increase the excitability of the AIS (Moore et al., 1983), when the axon is myelinated (Baranauskas et al., 2013). Therefore, in neurons with myelinated axons it is even more likely that AP initiation remains at the AIS despite a drop in the local density of ion channels. The computational model that we use here had been designed to capture AP initiation in pyramidal neurons and features myelinated axon sections, yet it replicates our experimental observations and thereby further supports the generality of our findings.

Previous theoretical studies generated diverse views on the relevance of a high channel density in the AIS. A very early multi-compartment model study (Moore et al., 1983) found that thanks to a lower capacitive load in the AIS, APs are initiated in the proximal axon, even when the local channel density is no higher than in the soma. In stark contrast later, more detailed computational models repeatedly found that a high density is required for axonal initiation (Kole et al., 2008; Mainen et al., 1995).

The relevance of axonal Na channel properties for encoding had been postulated through computational models of different complexity (Fourcaud-Trocme et al., 2003; Ilin et al., 2013), however, our study provides the first experimental manipulation restricted to the AIS, which decrease the timing precision of APs. An earlier study addressing this subject utilized the developmental change in AIS properties (Ilin et al., 2013). This is problematic as the concomitant increase in somato-dendritic size by itself also leads to a more rapid onset and higher encoding bandwidth (Eyal et al., 2014). The focal application of TTX is equally problematic, as it results in an imbalance between potassium and sodium current, which likely alter onset dynamics much more severe than a balanced reduction of both conductances. Furthermore, despite aiming for a focal Nav block, Ilin and colleagues report changes of somatic AP features, which might indicate that somatic channels were also affected. Our analysis (Fig. 2) indicates that there are no somatic aberrations in qV^{3J} .

While our experimental methods provide a quantitative assessment of channel densities, some information on the axonal sodium channels remains unknown. The pan-Nav antibody was used because of its superior signal to noise but it provides no information about the subtype of Navs. We cannot excluded, that the ration of Nav1.2 and Nav1.6 changes as a consequence of the qv^{3J} mutation. One could also speculate on an indirect effect of β IV-spectrin on functional properties of the Nav-channels, mediated through CaMKII. This kinase has been shown to influence cardiac sodium channels and is not correctly targeted to the AIS in the qv^{3J} mutant (Hund et al., 2010). While subtype composition and post-translational modifications might contribute to an altered excitability of the AIS, our conclusions are not affected by these unknowns. In fact the modelling suggests that the observed reduction of the encoding bandwidth is dominantly, if not exclusively, driven by the drop in channel density while the AIS maintains high excitability despite the density reduction, even if Nav properties remain constant.

An interesting parallel can be drawn between our finding and a recent study (Yang et al., 2016) on spike timing precision of neurons in the auditory pathway involved in inter-aural time detection, which fire non-overshooting APs (Golding et al., 1995; Oertel, 1983; Scott et al., 2005). These neurons achieve reliable and extremely precise AP initiation through a leaky soma with a low sodium channel concentration (Kuba et al., 2006; Yang et al., 2016). When the effective somatic sodium channel density was artificially increased to turn the soma more excitable, AP timing was degraded (Yang et al., 2016). In both cases, Yang et al. and our study, AP precision is improved if the AIS excitability is increased relative to the somatic excitability, i.e. the more independent axonal initiation can be from the electric load of the soma and the reverberations of previous activity and somatic input.

In contrast to the consensus in the field (reviewed in (Kole and Stuart, 2012), but see (Baranauskas et al., 2013)), we found that high axonal channel density is not crucial for an axonal locus of AP initiation. Instead, axonal AP initiation occurs even after drastic reduction of the axonal channel density, evident from electrophysiological recordings

combined with immunostaining and numerical modeling. Presumably, the spatial separation from the capacitive and resistive of the soma and the left-shifted activation curve of axonal sodium channels assure axonal initiation. To the best of our knowledge, the question whether a high axonal channel density is actually a requirement for axonal AP initiation has never been posed experimentally. Instead the differences between somatic and axonal channel densities that had been observed in some studies (Bender and Trussell, 2009; Fleidervish et al., 2010) but not others (Colbert and Johnston, 1996; Colbert and Pan, 2002) was simply assumed to be crucial for axonal AP initiation. Some support for this notion came from a multi-compartment model (Kole et al., 2008). However, similar to our results, a reduction of AIS densities in this model did not shift the initiation site into the soma. Instead, Kole and colleagues observed AP initiation in the nodes of Ranvier, if the channel density there was not reduced. Given the homologous molecular composition of nodes and AIS; and previous reports of reduced channel densities in qv^{3J} nodes (Devaux, 2010; Yang et al., 2004), we reduced channel densities throughout the model's axon and consequently the AIS remained the most excitable section even for a 20 fold decrease in channel densities.

Following a complete loss of mutant spectrin from the AIS until 10 DIV, the local densities of Nav and AnkG slowly drop below the detection limit of immunocytochemistry over the next several days. This delay indicates that β IV-spectrin is not the only anchor for these proteins, possibly they are retained through binding to the membrane, sodium channel beta subunits, β II-spectrin or other AIS proteins. In brain tissue the compensatory effect of β II-spectrin and other components seems to last longer than in cell cultures, a study by Yang and colleagues (2007) demonstrate detectable levels of AnkG and pan-Nav labelling in qv^{3J} mice at 6 month of age. Interestingly, in our study Nav densities drop more rapidly than AnkG densities. This is not captured in a simple model, where Nav recruitment to the AIS is dominated by AnkG.

Our analysis of single molecule localization microscopy for AnkG, pan-Nav (Fig. 4), β II-spectrin (Fig. 7) and β IV-spectrin in control animals (not shown) confirms previous studies reporting a highly regular cytoskeleton in the AIS. Although β IV-spectrin is considered to be a central component of this cytoskeleton (Zhong et al., 2014), we found no indication for loss of regularity of AnkG and Nav channels in the qv^{3J} mutant. Apparently, β II-spectrin is sufficient to maintain the spatial arrangement of AIS proteins throughout maturation. This suggests that the perturbation of AIS manifests mainly in a reduction of protein copy numbers, rather than their arrangement within the AIS nanostructure. If other mutations could obtain an orthogonal result, a perturbation of the regular cytoskeleton without reduction of channel numbers, the functional relevance of the nanostructure could be elucidated.

Methods

Cell culture

Hippocampi were isolated from newborn (P0) qv^{3J} mice, collected in a serum-free Neurobasal-A medium (Life Technologies, 12349-015) with 100 mM HEPES buffer solution (Life Technologies, 15630-056) and digested with trypsin/EDTA 0.05%/0.02% (w/v, Biochrom) in PBS for 12 minutes at 37°C. The hippocampi were then transferred to Neurobasal-A medium, pipetted up and down for homogenization, and centrifuged for 2 minutes. Hippocampi from each newborn offspring were used to prepare a separate culture. For electrophysiology measurements and wide-field imaging, cells from the hippocampi of each newborn mouse were plated in one 8.8cm² cell culture dish (Nunclon, 153066), on 7 glass cover slips (Thermo Scientific, Menzel-Glaeser 10 mm #1), coated with 0.1 mg/ml poly-L-lysine (Sigma-Aldrich, P2636), in 2 ml Neurobasal-A medium supplemented with 1:50 B27 (Life Technologies, 17504-044), 1:400 glutamax (Life Technologies, 35050-038) and 0.01 μ g/mL fibroblast growth factor (b-FGF, Life Technologies, 13256-029). For dSTORM imaging, the cells were seeded in 4-well tissue culture chambers on cover glass

(Sarstedt 94.61990.402), one hippocampus per well, in supplemented medium. Cultures were kept in an incubator at 37°C in a humidified atmosphere of 95% air and 5% CO₂. One half of the culture medium was changed weekly with freshly prepared medium. Tail biopsies were used for genotyping and were afterwards related with the corresponding culture.

Genotyping

Mice were genotyped by PCR on tail biopsy samples using the following primers: forward, 5'-AGG CAG CGC CTT TGC TGC GTC-3'; reverse, 5'-TCC TGG TCA CAG AGG TCC TTA-3'. PCR mix contained 1.0 µl DNA, 0.2 µl of each primer, 0.4 µl DreamTaq DNA Polymerase (Thermo Scientific, EP0703), and PCR buffer (containing Tris-HCl (pH 8.8), ammonium sulphate (Sigma), MgCl₂ (Sigma- Aldrich), 2-mercaptoethanol (Merck), EDTA (pH 8.0) (Sigma), nucleoside triphosphates (dATP, dCTP, dGTP, dTTP) (Promega), BSA (Ambion - Life Technologies) and H₂O to final volume of 20 µl). PCR conditions were: 3 minutes of initial denaturation at 94°C, followed by 36 cycles of 30 seconds denaturation at 94°C, 30 seconds annealing at 60°C, and 60 seconds elongation at 72°C. Final elongation was performed for 7 minutes at 72°C. Enzymatic digestion was performed with StyI (10 U/µl) (New England Biolabs, R0500S). The PCR product was separated by 3% gel electrophoresis (+/+ 600 bp, +/- 600 bp + 350 bp + 250 bp, -/- 350 bp + 250 bp).

Electrophysiology

Whole cell recordings were performed in cells from cultures at different developmental stages *in vitro*. Extracellular medium contained (in mM) 134 NaCl, 4 KCl, 2 CaCl₂, 1 MgCl₂, 10 HEPES, and 20 glucose (pH 7.4 with NaOH, 290 mOsm). Synaptic blockers against AMPA, GABA-a and NMDA receptors (10 µM NBQX, 50 µM Picrotoxin and 100 µM APV) were added to the medium, and completely suppressed synaptic input and also abolished spontaneous activity in the culture. Patch pipettes were fabricated from

PG10165-4 glass (World Precision Instruments) and contained K-gluconate based intracellular solution consisting of (in mM): 136 K- gluconate, 10 KCl, 5 NaCl, 0.1 EGTA, 1 MgATP, 0.3 NaGTP, 10 HEPES and 5 Phosphocreatine (pH 7.3 with KOH, 300 mOsm). Pipette resistance varied between 3 and 6 MOhm, yielding access resistances between 5 and 15 MOhm. In some experiments 100 μ M (final concentration) Alexa 568 hydrazide (sodium salt, Life Technologies, A-10437) was added to the intracellular solution (Figs. xxx and S4). Whole cell patch clamp was performed at room temperature (26°C) using an EPC10 amplifier controlled by Patchmaster (both HEKA Elektronik). The recordings were sampled at 100 KHz (step pulses) or 50 KHz (fluctuating input). Appropriate bridge and electrode capacitance compensation was applied. Using Patcher's Power Tools (Dr. Francisco Mendez, Frank Würriehausen) the recordings were imported into Igor Pro (Wavemetrics) and analyzed with custom written routines. Measurements were corrected for calculated liquid junction potential (LJP) of 16 mV.

Current stimuli

The subthreshold membrane properties and the characteristics of the action potential were obtained by injecting a series of 100 ms long current steps with increasing amplitudes. Between stimuli, the neurons were held for 5s at -76 mV (LJP corrected). For the data in Fig. 2, we analyzed the APs recorded for the smallest suprathreshold current for which an AP was generated within 10 ms after current onset.

Frequency response properties were investigated using input currents synthesized as Ornstein-Uhlenbeck (OU) noise with zero mean and correlation time of 35 ms. The stimulus was applied for 50 s in 5 trials, separated by 60-90 s intervals in which the cell was held at -76 mV. In each trial, the stimulus was generated with similar mean and standard deviation but different random seed (i.e. different initial values of the internal state of the random number generator). The same 5 realizations of the noise, created by the same set of random seeds, were used for the different cells. The standard deviation of the injected current was adjusted for each cell to achieve a firing rate of 2 - 3 Hz while the DC

component was adjusted to warrant a membrane potential fluctuating around -60 mV. For most cells this DC component was no more than 20 pA.

Dynamic gain calculation

The frequency transfer function was calculated from responses to injected fluctuating current, using a method originally introduced by Bryant and Segundo (Bryant and Segundo, 1976) with modifications. AP time was registered when the somatic membrane voltage crossed 3mV, which corresponds to the steepest point on the AP waveform. The spike triggered average (STA) current was calculated for each cell from ~ 600 spikes by averaging stimulus waveform in a temporal window of 500 ms before and after the spike. To improve signal-to-noise ratio, the STA was filtered in the frequency domain using a Gaussian window $w(f')$, centered at frequency $f' = f$, with an SD of $f/2\pi$,

$$w(f') = \frac{1}{\sqrt{2\pi} \cdot \left(\frac{f}{2\pi}\right)} \cdot \exp\left[-\frac{1}{2}\left(\frac{f' - f}{f/2\pi}\right)^2\right]$$

This averages out neighboring frequency components of similar amplitude but random phase, i.e. noise. Deterministic frequency components with a phase that changes only mildly within the Gaussian window are not affected by this windowing. Thus,

$$STA_w(f) = \frac{\int STA(f') \cdot w(f') \cdot df'}{\int w(f') \cdot df'}$$

If the train of APs is idealized as a discrete sequence of numbers with zero for empty samples and $1/dt$ for samples carrying an AP, then the product of the STA current and the firing rate ν equals the cross-correlation between input current and AP output. The frequency response function (or the dynamic gain), $G(f)$, was then calculated as the ratio between the Fourier transform of this cross correlation $\widetilde{CC_{I \leftrightarrow AP}}$ and the Fourier transform of the auto-correlation of the input current $\widetilde{AC_I}$. The later is equal to the power spectral

density (PSD) of the input current and for an OU process, the analytical expression of the PSD can replace the numerical auto-correlation.

$$G(f) = \frac{|STA_w(f)| \cdot \bar{\nu}}{PSD(f)} = \frac{C \widetilde{C_{I \leftrightarrow AP}}}{\widetilde{A C_I}}$$

$$PSD(f) = \widetilde{A C_I} = \frac{4 \tau_{corr} \sigma^2}{1 + (2\pi f \tau_{corr})^2}$$

Where σ is the standard deviation of the input current and τ_{corr} is the correlation time of the noise.

To average the gain curves from N cells, we averaged the STA currents. To avoid over-representation of cells with a smaller input resistance, i.e. cells that require a larger amplitude of current fluctuations, we weighted the STA curves: $\overline{STA} = \frac{1}{N} \cdot \sum_{i=1}^N STA_i \cdot \frac{\bar{\sigma}}{\sigma_i^2}$ with the average input variance $\bar{\sigma} = \frac{1}{N} \cdot \sum_{i=1}^N \sigma_i^2$. The average cross-correlation was obtained by multiplication with the average firing rate:

$$\bar{\nu} = \frac{\sum_{i=1}^N n_i^{APs}}{\sum_{i=1}^N T_i^{rec.}}$$

The average gain is thus

$$\overline{G(f)} = \frac{|\overline{STA}_w \cdot \bar{\nu}|}{\frac{4\tau_{corr}\bar{\sigma}}{1 + (2\pi f \tau_{corr})^2}}$$

For each neuron and for the population average we calculated the confidence intervals of the gain curve as well as the noise floor by balanced bootstrap. The confidence interval at a given frequency f' was defined by the 5th and the 95th percentile of $G_{BST}(f')$ for 200 bootstrap gain curves calculated from 200 random samples of actual AP times. The noise floor at a certain frequency is understood as 95th percentile of $G_{BST}^{rnd}(f')$ calculated not from measured but from random AP times. To obtain random AP times without changing the statistics of the AP time series, we applied a cyclic shift of the injected current by a random

value larger than 5 correlation times. This results in a random triggered average of the input which replaces the STA current in the calculations for G_{BST}^{rnd} .

Conditional firing rate

Each neuron in the dataset of dynamic gain and conditional firing rate analysis was stimulated with the same five stochastically changing current stimuli I^1 to I^5 (see above: current stimuli), only the fluctuation amplitude was adjusted between neurons to achieve firing rates of approximately 2 Hz. A given neuron m fires the AP sequences s_m^1 to s_m^5 in response to those stimuli. The conditional firing rate between neurons m and k is defined as the average over the conditional firing rates of the five trials:

$$v_{cond\ m,k}(\tau) = (v_m \cdot v_k)^{-1/2} \sum_{i=1}^5 \langle s_m^i(t) \cdot s_k^i(t + \tau) \rangle$$

To obtain the average conditional firing rate of the neurons from control of mutant mice,

we averaged: $v_{cond}(\tau) = \frac{2}{N_{cells} \cdot (N_{cells} - 1)} \sum_{m=2}^{N_{cells}} \sum_{k=1}^{m-1} v_{cond\ m,k}(\tau)$

Action potential characterization

The somatic AP waveform was characterized with the following set of parameters: the threshold voltage (V_{thresh}) was estimated as the value of the membrane potential when dV/dt crosses 25 V/s; the AP onset rapidness was calculated as the slope of the phase plot at the threshold voltage; the peak rate of rise was the peak value of dV/dt and peak potential was the peak value of V .

Great care was taken to properly compensate the fast capacitance since it has an influence on the shape of the phase plot is sensitive to the capacitance compensation.

Simulations

A multi-compartment model, developed by Hallermann and colleagues (2012) to capture the properties of AP generation in pyramidal neurons in brain slices, was used for the simulations of AP initiation and spike time precision (<https://senselab.med.yale.edu/modeldb/ShowModel.cshtml?model=144526>). The properties of all active conductances and their spatial distribution were left unchanged from the original model. To obtain the transfer functions for different axonal channel densities, many millions of seconds had to be simulated. To reduce the computational load, the model morphology was compacted: the basal dendrites and the apical dendritic branch and the initial axon were each represented by a single process with adjusted geometry, two axon collaterals are branching off the main axon. Compacting the morphology did not alter the characteristics of the model for AP waveform or transfer function, but greatly expedited simulations. For some simulations, we exchanged the somatic sodium channel model from Schmidt-Hieber and Bischofberger against a similar model we had derived from our own measurements, the AP waveforms and transfer functions changed only marginally, this version of the model was used for the results presented here.

To obtain the transfer function, the model is driven by somatic injection of a fluctuating current, derived from an Ornstein-Uhlenbeck process with correlation time 35 ms. The mean and standard deviation of the process are chosen to obtain a firing rate of 2 Hz and a coefficient of variation of the inter-spike interval around 0.85. This reflects a fluctuation-driven state and closely matches the experimentally obtained firing statistics. Each simulation is 200 s long with sample interval of 0.025 ms, 250 such 200 s simulation are combined to obtain approximately 10^6 spikes for each set of axonal channel densities. AP time is set when the somatic voltage crosses +8 mV. From AP times and the input current we calculate the spike triggered average input (STA input), which represents the cross-correlation of input and AP output. The transfer function TF is calculated as the ratio of the Fourier transformations of the cross-correlation (STA input) multiplied with the firing

rate f and the auto-correlation of the input. The latter corresponds to the power spectral density (PSD) of the input: $TF = \frac{FFT(STA) \cdot v}{PSD_{OU}}$

Immunocytochemistry

Neurons were washed twice in PBS and fixed with 4% formaldehyde in PBS for 8 minutes at 4°C and then washed in PBS. Permeabilization was performed by 5-minute incubation with 0.5% Triton X-100 in PBS, followed by 5-minute incubation with 0.1% Tween in PBS. The cells were then incubated for 1.5 hours in 3% BSA and 0.1% Tween in PBS (blocking solution) and then in primary antibody diluted in blocking solution at 4 °C, overnight. After washing, secondary antibodies were diluted in blocking solution and applied for 45 minutes. For wide-field imaging, the coverslips were mounted on microscope slides using Prolong Gold antifade with or without DAPI (Life Technologies, P36935 or P36930). For dSTORM imaging, the cells were post fixated with 4% formaldehyde in PBS for 5 minutes, washed 3 times with PBS and stored with PBS at 4 °C.

The primary antibodies that were employed in this study were: mouse monoclonal anti-sodium channel (Pan-Nav) 1:900 (Clone K58/35; Sigma-Aldrich, S8809-1MG), goat polyclonal anti-βIV spectrin antibody 1:200 (ORIGene, TA317365, targeting N-terminal sequence aa2-14), rabbit polyclonal anti-βIV spectrin antibody 1:200 (ATLAS, HPA043370, targeting a centrally located sequence), rabbit polyclonal anti-AnkG antibody 1:200 (Santa Cruz Biotechnology, sc-28561, targeting C-terminal sequence), mouse monoclonal anti-AnkG antibody 1:200 (Santa Cruz Biotechnology, sc-12719, targeting N-terminal sequence), chicken polyclonal anti-Map2 1:2000 (Abcam, ab5392), mouse monoclonal anti-βII spectrin 1:200 (Santa Cruz Biotechnology, sc-136074) .

The following secondary antibodies were used (1:1000). For wide-field imaging: Alexa Fluor 488 goat anti-mouse (Life Technologies, A11029), Alexa Fluor 647 donkey anti-goat (Life Technologies, A21447, Alexa Fluor 488 goat anti-rabbit (Jackson ImmunoResearch 111-545-003), Alexa Fluor 647 goat anti-rabbit (Life Technologies, A21245), Alexa Fluor 647 goat anti-chicken (Life Technologies, A214469), Alexa 488

Donkey anti-chicken (Jackson ImmunoResearch 703-545-155). For dSTORM imaging: Alexa Fluor 647 goat anti-mouse (Life Technologies, A21236).

Wide-Field imaging

Images were recorded using an inverted widefield microscope (Olympus IX-71) equipped with a water-immersion objective lens (UPlanSApo, 60x magnification, NA 1.2, Olympus). Violet (emission maximum at 390 nm), cyan (emission maximum at 475 nm), yellow (emission maximum at 603 nm) and red (emission maximum at 634 nm) LEDs (Spectra X light engine, Lumencor) were used for excitation of DAPI, Alexa 488, Alexa 568 and Alexa 647, respectively. The fluorescence light was separated from the LED light with a dichroic beam splitter (59004bs, Chroma Technologies) and additional excitation filters (BLP01-405R, Semrock for DAPI; FF01-520/35, Semrock for Alexa 488; and BLP01-594R Semrock for Alexa 568, BLP01-635R Semrock for Alexa 647) before being imaged on an electron multiplying CCD camera (EMCCD; DU-897-CS0-BV, Andor) with an effective pixel size of 160 nm; temperature of detector -50 °C.

Images were analyzed using the image line profile operation (with line width of 5 pixels) Igor Pro (Wavemetrics). Units refer to CCD pixel readout under strictly constant settings and parameters for immunostaining and imaging protocols within a dataset. “Arbitrary” units refers solely to the fact that the CCD’s readout magnitude is arbitrary *overall*, but not within or between measurements. Specifically it is not possible to compare fluorescence intensity units between different antibodies or detection protocols (STORM and widefield), but as the confidence intervals on repeated measurements with identical antibody batches and identical staining and imaging protocols show, there is good comparability within those measurements (Fig S3).

dSTORM imaging

The imaging buffer used was 10 mM TRIS containing 100 mM cysteamine hydrochloride (Sigma-Aldrich, M6500), 4.0 mg/mL glucose oxidase (Sigma-Aldrich, G0543), 0.57 mg/mL catalase (Sigma-Aldrich, C40-100MG), and 10 % glucose (Sigma-Aldrich, 49158-

1KG-F). pH was adjusted with 0.5 M NaOH to pH 8.3-8.5. Chamber wells were completely filled with buffer and sealed bubble-free (air-free) by a regular coverslip. Images were recorded using an inverted TIRF microscope (Olympus IX-71) equipped with an oil-immersion objective lens (Olympus, UApoN, 100x magnification, NA 1.49, TIRF) and a 647 nm laser (PhoxX 647, 140 mW, Omicron Laserage, Germany). A quad-edge dichroic beam splitter (Di01-R405/488/561/635, Semrock) and a quad-band excitation filter (FF01-446/523/600/ 677, Semrock) were used to remove the laser light before imaging the fluorescence on an electron multiplying CCD camera cooled to -50°C (EMCCD; DU-885-CS0-#VP, Andor) with an effective pixel size of 80 nm. Raw movies typically contained 3000 - 4000 images recorded at 30 - 90Hz. Images were analyzed using rapidSTORM and custom written routines in Matlab.

References

- Baranauskas, G., David, Y., Fleidervish, I.A., 2013. Spatial mismatch between the Na⁺ flux and spike initiation in axon initial segment. *Proc. Natl. Acad. Sci.* doi:10.1073/pnas.1215125110
- Bender, K.J., Trussell, L.O., 2009. Axon initial segment Ca²⁺ channels influence action potential generation and timing. *Neuron* 61, 259–271. doi:10.1016/j.neuron.2008.12.004
- Bennett, V., Baines, A.J., 2001. Spectrin and Ankyrin-Based Pathways: Metazoan Inventions for Integrating Cells Into Tissues. *Physiol. Rev.* 81, 1353–1392.
- Berghs, S., Aggujaro, D., Dirkx, R., Maksimova, E., Stabach, P., Hermel, J.-M., Zhang, J.-P., Philbrick, W., Slepnev, V., Ort, T., Solimena, M., 2000. β IV Spectrin, a New Spectrin Localized at Axon Initial Segments and Nodes of Ranvier in the Central and Peripheral Nervous System. *J. Cell Biol.* 151, 985–1002. doi:10.1083/jcb.151.5.985
- Boucsein, C., Tetzlaff, T., Meier, R., Aertsen, A., Naundorf, B., 2009. Dynamical Response Properties of Neocortical Neuron Ensembles: Multiplicative versus Additive Noise. *J. Neurosci.* 29, 1006–1010. doi:10.1523/JNEUROSCI.3424-08.2009
- Brette, R., 2013. Sharpness of Spike Initiation in Neurons Explained by Compartmentalization. *PLoS Comput Biol* 9, e1003338. doi:10.1371/journal.pcbi.1003338
- Bryant, H.L., Segundo, J.P., 1976. Spike initiation by transmembrane current: a white-noise analysis. *J. Physiol.* 260, 279–314.
- Colbert, C.M., Johnston, D., 1996. Axonal Action-Potential Initiation and Na⁺ Channel Densities in the Soma and Axon Initial Segment of Subicular Pyramidal Neurons. *J. Neurosci.* 16, 6676–6686.
- Colbert, C.M., Pan, E., 2002. Ion channel properties underlying axonal action potential initiation in pyramidal neurons. *Nat Neurosci* 5, 533–538. doi:10.1038/nn0602-857
- Devaux, J.J., 2010. The C-terminal domain of β IV-spectrin is crucial for KCNQ2 aggregation and excitability at nodes of Ranvier. *J. Physiol.* 588, 4719–4730. doi:10.1113/jphysiol.2010.196022
- Eyal, G., Mansvelder, H.D., Kock, C.P.J. de, Segev, I., 2014. Dendrites Impact the Encoding Capabilities of the Axon. *J. Neurosci.* 34, 8063–8071. doi:10.1523/JNEUROSCI.5431-13.2014

- Fleiderovich, I.A., Lasser-Ross, N., Gutnick, M.J., Ross, W.N., 2010. Na⁺ imaging reveals little difference in action potential-evoked Na⁺ influx between axon and soma. *Nat Neurosci* 13, 852–860. doi:10.1038/nn.2574
- Fourcaud-Trocme, N., Hansel, D., van Vreeswijk, C., Brunel, N., 2003. How Spike Generation Mechanisms Determine the Neuronal Response to Fluctuating Inputs. *J. Neurosci.* 23, 11628–11640.
- Golding, N., Robertson, D., Oertel, D., 1995. Recordings from slices indicate that octopus cells of the cochlear nucleus detect coincident firing of auditory nerve fibers with temporal precision. *J. Neurosci.* 15, 3138–3153.
- Hallermann, S., Kock, C.P.J. de, Stuart, G.J., Kole, M.H.P., 2012. State and location dependence of action potential metabolic cost in cortical pyramidal neurons. *Nat. Neurosci.* 15, 1007–1014. doi:10.1038/nn.3132
- Hedstrom, K.L., Ogawa, Y., Rasband, M.N., 2008. AnkyrinG Is Required for Maintenance of the Axon Initial Segment and Neuronal Polarity. *J. Cell Biol.* 183, 635–640. doi:10.1083/jcb.200806112
- Higgs, M.H., Spain, W.J., 2009. Conditional Bursting Enhances Resonant Firing in Neocortical Layer 2-3 Pyramidal Neurons. *J. Neurosci.* 29, 1285–1299. doi:10.1523/JNEUROSCI.3728-08.2009
- Hu, W., Tian, C., Li, T., Yang, M., Hou, H., Shu, Y., 2009. Distinct contributions of Nav1.6 and Nav1.2 in action potential initiation and backpropagation. *Nat Neurosci* 12, 996–1002. doi:10.1038/nn.2359
- Hund, T.J., Koval, O.M., Li, J., Wright, P.J., Qian, L., Snyder, J.S., Gudmundsson, H., Kline, C.F., Davidson, N.P., Cardona, N., Rasband, M.N., Anderson, M.E., Mohler, P.J., 2010. A β (IV)-spectrin/CaMKII signaling complex is essential for membrane excitability in mice. *J. Clin. Invest.* 120, 3508–3519. doi:10.1172/JCI43621
- Ilin, V., Malyshev, A., Wolf, F., Volgushev, M., 2013. Fast Computations in Cortical Ensembles Require Rapid Initiation of Action Potentials. *J. Neurosci.* 33, 2281–2292. doi:10.1523/JNEUROSCI.0771-12.2013
- Jenkins, S.M., Bennett, V., 2001. Ankyrin-G coordinates assembly of the spectrin-based membrane skeleton, voltage-gated sodium channels, and L1 CAMs at Purkinje neuron initial segments. *J. Cell Biol.* 155, 739–746. doi:10.1083/jcb.200109026
- Kole, M.H.P., Ilschner, S.U., Kampa, B.M., Williams, S.R., Ruben, P.C., Stuart, G.J., 2008. Action potential generation requires a high sodium channel density in the axon initial segment. *Nat. Neurosci.* 11, 178–186. doi:10.1038/nn2040
- Kole, M.H.P., Stuart, G.J., 2012. Signal Processing in the Axon Initial Segment. *Neuron* 73, 235–247. doi:10.1016/j.neuron.2012.01.007
- Komada, M., Soriano, P., 2002. β (IV)-spectrin regulates sodium channel clustering through ankyrin-G at axon initial segments and nodes of Ranvier. *J Cell Biol* 156, 337–348. doi:10.1083/jcb.200110003
- Kondgen, H., Geisler, C., Fusi, S., Wang, X.-J., Luscher, H.-R., Giugliano, M., 2008. The Dynamical Response Properties of Neocortical Neurons to Temporally Modulated Noisy Inputs In Vitro. *Cereb Cortex* 18, 2086–2097. doi:10.1093/cercor/bhm235
- Kuba, H., Ishii, T.M., Ohmori, H., 2006. Axonal site of spike initiation enhances auditory coincidence detection. *Nature* 444, 1069–1072. doi:10.1038/nature05347
- Lacas-Gervais, S., Guo, J., Strenzke, N., Scarfone, E., Kolpe, M., Jahkel, M., Camilli, P.D., Moser, T., Rasband, M.N., Solimena, M., 2004. β IV Σ 1 spectrin stabilizes the nodes of Ranvier and axon initial segments. *J. Cell Biol.* 166, 983–990. doi:10.1083/jcb.200408007
- Letierrier, C., Potier, J., Caillol, G., Debarnot, C., Rueda Boroni, F., Dargent, B., 2015. Nanoscale Architecture of the Axon Initial Segment Reveals an Organized and Robust Scaffold. *Cell Rep.* 13, 2781–2793. doi:10.1016/j.celrep.2015.11.051

- Lorincz, A., Nusser, Z., 2010. Molecular Identity of Dendritic Voltage-Gated Sodium Channels. *Science* 328, 906–909. doi:10.1126/science.1187958
- Mainen, Z.F., Joerges, J., Huguenard, J.R., Sejnowski, T.J., 1995. A model of spike initiation in neocortical pyramidal neurons. *Neuron* 15, 1427–1439. doi:10.1016/0896-6273(95)90020-9
- Moore, J.W., Stockbridge, N., Westerfield, M., 1983. On the site of impulse initiation in a neurone. *J. Physiol.* 336, 301–311. doi:10.1113/jphysiol.1983.sp014582
- Naundorf, B., Geisel, T., Wolf, F., 2005. Action potential onset dynamics and the response speed of neuronal populations. *J. Comput. Neurosci.* 18, 297–309. doi:10.1007/s10827-005-0329-8
- Naundorf, B., Wolf, F., Volgushev, M., 2006. Unique features of action potential initiation in cortical neurons. *Nature* 440, 1060–1063. doi:10.1038/nature04610
- Oertel, D., 1983. Synaptic responses and electrical properties of cells in brain slices of the mouse anteroventral cochlear nucleus. *J. Neurosci.* 3, 2043–2053.
- Ogawa, Y., Schafer, D.P., Horresh, I., Bar, V., Hales, K., Yang, Y., Susuki, K., Peles, E., Stankewich, M.C., Rasband, M.N., 2006. Spectrins and AnkyrinB Constitute a Specialized Paranodal Cytoskeleton. *J. Neurosci.* 26, 5230–5239. doi:10.1523/JNEUROSCI.0425-06.2006
- Ostojic, S., Szapiro, G., Schwartz, E., Barbour, B., Brunel, N., Hakim, V., 2015. Neuronal Morphology Generates High-Frequency Firing Resonance. *J. Neurosci.* 35, 7056–7068. doi:10.1523/JNEUROSCI.3924-14.2015
- Parkinson, N.J., Olsson, C.L., Hallows, J.L., McKee-Johnson, J., Keogh, B.P., Noben-Trauth, K., Kujawa, S.G., Tempel, B.L., 2001. Mutant β -spectrin 4 causes auditory and motor neuropathies in quivering mice. *Nat. Genet.* 29, 61–65. doi:10.1038/ng710
- Rasband, M.N., 2010. The axon initial segment and the maintenance of neuronal polarity. *Nat Rev Neurosci* 11, 552–562. doi:10.1038/nrn2852
- Scott, L.L., Mathews, P.J., Golding, N.L., 2005. Posthearing developmental refinement of temporal processing in principal neurons of the medial superior olive. *J. Neurosci. Off. J. Soc. Neurosci.* 25, 7887–7895. doi:10.1523/JNEUROSCI.1016-05.2005
- Shinomoto, S., Kim, H., Shimokawa, T., Matsuno, N., Funahashi, S., Shima, K., Fujita, I., Tamura, H., Doi, T., Kawano, K., Inaba, N., Fukushima, K., Kurkin, S., Kurata, K., Taira, M., Tsutsui, K.-I., Komatsu, H., Ogawa, T., Koida, K., Tanji, J., Toyama, K., 2009. Relating Neuronal Firing Patterns to Functional Differentiation of Cerebral Cortex. *PLOS Comput Biol* 5, e1000433. doi:10.1371/journal.pcbi.1000433
- Tchumatchenko, T., Malyshev, A., Wolf, F., Volgushev, M., 2011. Ultra-fast population encoding by cortical neurons. *J. Neurosci.* 31, 12171–9. doi:10.1523/JNEUROSCI.2182-11.2011
- Tchumatchenko, T., Wolf, F., 2011. Representation of Dynamical Stimuli in Populations of Threshold Neurons. *PLoS Comput Biol* 7, e1002239. doi:10.1371/journal.pcbi.1002239
- Testa-Silva, G., Verhoog, M.B., Linaro, D., de Kock, C.P.J., Baayen, J.C., Meredith, R.M., De Zeeuw, C.I., Giugliano, M., Mansvelder, H.D., 2014. High Bandwidth Synaptic Communication and Frequency Tracking in Human Neocortex. *PLoS Biol.* 12. doi:10.1371/journal.pbio.1002007
- Uemoto, Y., Suzuki, S., Terada, N., Ohno, N., Ohno, S., Yamanaka, S., Komada, M., 2007. Specific Role of the Truncated β IV-Spectrin Σ 6 in Sodium Channel Clustering at Axon Initial Segments and Nodes of Ranvier. *J. Biol. Chem.* 282, 6548–6555. doi:10.1074/jbc.M609223200
- van de Linde, S., Löschberger, A., Klein, T., Heidbreder, M., Wolter, S., Heilemann, M., Sauer, M., 2011. Direct stochastic optical reconstruction microscopy with standard fluorescent probes. *Nat. Protoc.* 6, 991–1009. doi:10.1038/nprot.2011.336
- Wei, W., Wolf, F., 2011. Spike onset dynamics and response speed in neuronal populations. *Phys. Rev. Lett.* 106, 088102. doi:10.1103/PhysRevLett.106.088102
- Xu, K., Zhong, G., Zhuang, X., 2013. Actin, Spectrin, and Associated Proteins Form a Periodic Cytoskeletal Structure in Axons. *Science* 339, 452–456. doi:10.1126/science.1232251

- Xu, M., Cooper, E.C., 2015. An Ankyrin-G N-terminal Gate and Protein Kinase CK2 Dually Regulate Binding of Voltage-gated Sodium and KCNQ2/3 Potassium Channels. *J. Biol. Chem.* 290, 16619–16632. doi:10.1074/jbc.M115.638932
- Yang, Y., Lacas-Gervais, S., Morest, D.K., Solimena, M., Rasband, M.N., 2004. β IV Spectrins Are Essential for Membrane Stability and the Molecular Organization of Nodes of Ranvier. *J Neurosci* 24, 7230–7240. doi:10.1523/JNEUROSCI.2125-04.2004
- Yang, Y., Ogawa, Y., Hedstrom, K.L., Rasband, M.N., 2007. β IV spectrin is recruited to axon initial segments and nodes of Ranvier by ankyrinG. *J Cell Biol* 176, 509–519. doi:10.1083/jcb.200610128
- Yang, Y., Ramamurthy, B., Neef, A., Xu-Friedman, M.A., 2016. Low Somatic Sodium Conductance Enhances Action Potential Precision in Time-Coding Auditory Neurons. *J. Neurosci.* 36, 11999–12009. doi:10.1523/JNEUROSCI.1475-16.2016
- Yoshimura, T., Stevens, S.R., Leterrier, C., Stankewich, M.C., Rasband, M.N., 2017. Developmental Changes in Expression of β IV Spectrin Splice Variants at Axon Initial Segments and Nodes of Ranvier. *Front. Cell. Neurosci.* 10. doi:10.3389/fncel.2016.00304
- Zhong, G., He, J., Zhou, R., Lorenzo, D., Babcock, H.P., Bennett, V., Zhuang, X., n.d. Developmental mechanism of the periodic membrane skeleton in axons. *eLife* 3. doi:10.7554/eLife.04581
- Zhou, D., Lambert, S., Malen, P.L., Carpenter, S., Boland, L.M., Bennett, V., 1998. AnkyrinG is required for clustering of voltage-gated Na channels at axon initial segments and for normal action potential firing. *J. Cell Biol.* 143, 1295–1304.

SUPPLEMENTARY FIGURES

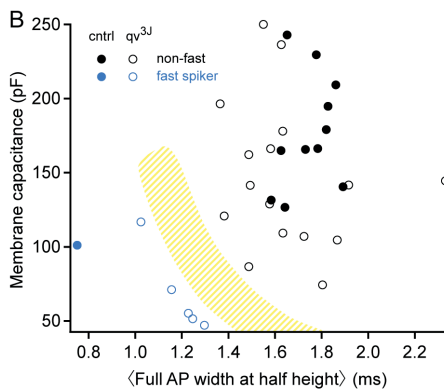


Figure S1: Identification of putative fast spiking neurons In cultures from control mice, fast spiking neurons were reliably identified by very brief APs, due to rapid repolarization. Examples can be seen in two phase plots in figure S2, DIV 39. In addition, fast spiking neurons tended to be relatively small, reflected in a small membrane capacitance. The population of neurons from mutant mice was slightly less homogeneous in their properties, therefore the fast spiking neurons were identified using a plot of membrane capacitance versus AP duration, measured as full width at half maximal depolarization. The hatched area in this plot separates neurons that are regarded as fast spiking neurons (lower left, 5 mutant 1 control) from neurons that are regarded as regular spiking neurons. This identification is supported by the neurons firing patterns in response to constant current injections (not shown).

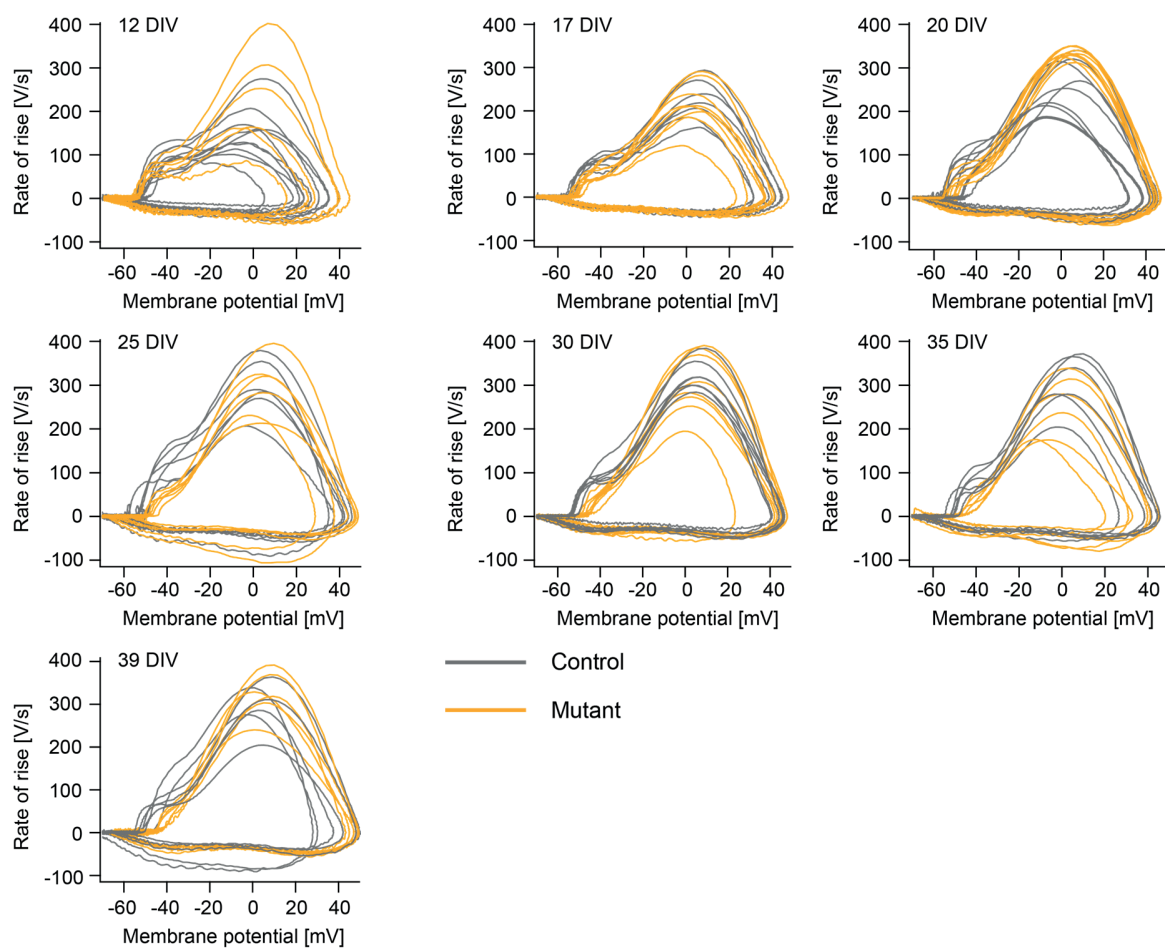


Figure S2: APs from qv^{3J} mutant neurons lose their rapid onset with maturation. Phase plane analysis of APs recorded from mutant (orange) and control (gray) cells between DIV 12 and 39 shows that at early developmental stage the AP waveform of mutant cells was biphasic as in control cells. Later during development the AP onset in mutant cells became slower and the biphasic shape was lost in an increasingly large fraction of cells. The cultures used for this data series are from a single preparation (i.e. one litter). In each plot the APs were recorded on the same day under identical conditions from the different cultures. Cell population included regular- as well as fast-spiking neurons, which can be distinguished by their faster repolarization rate.

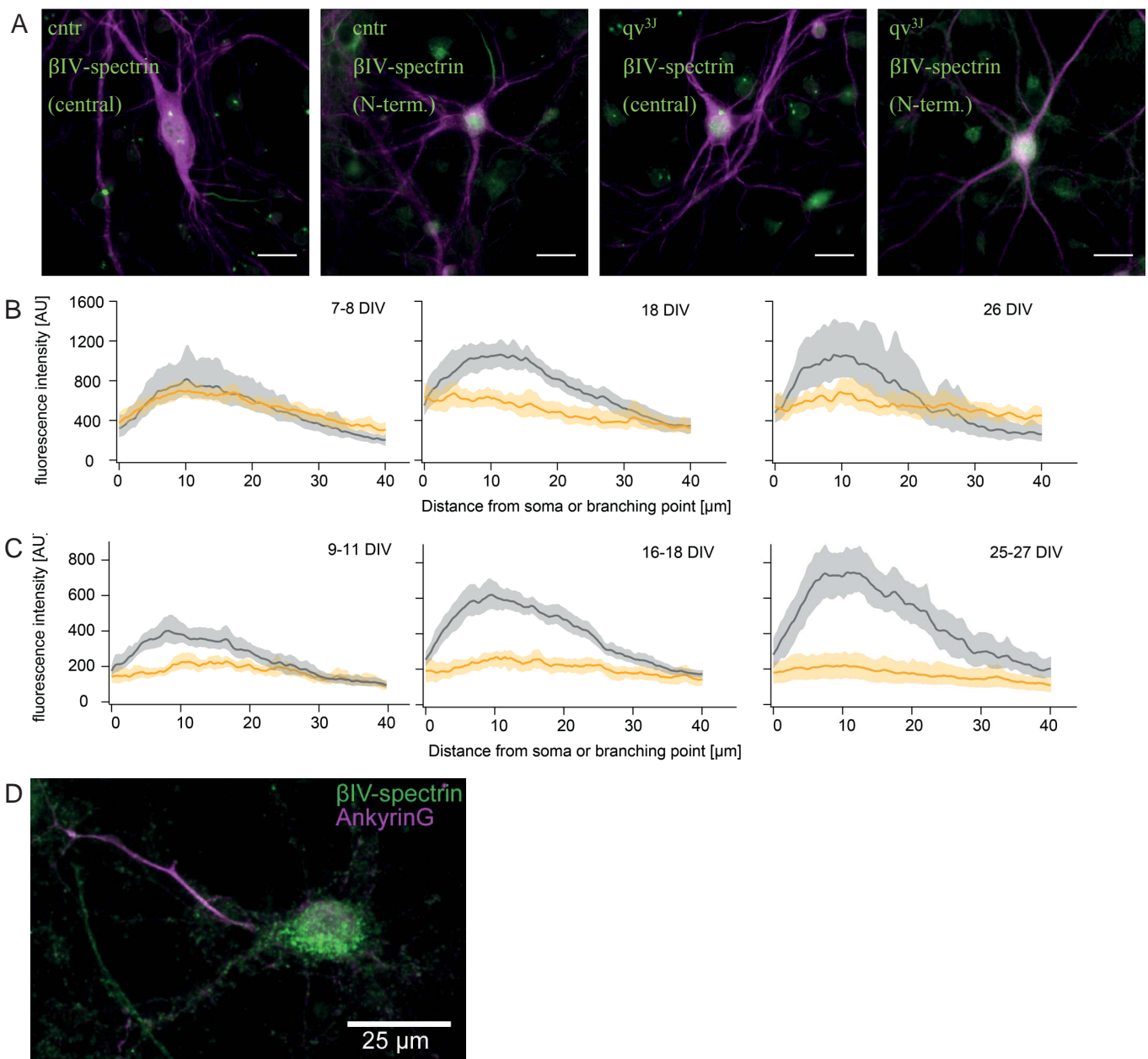
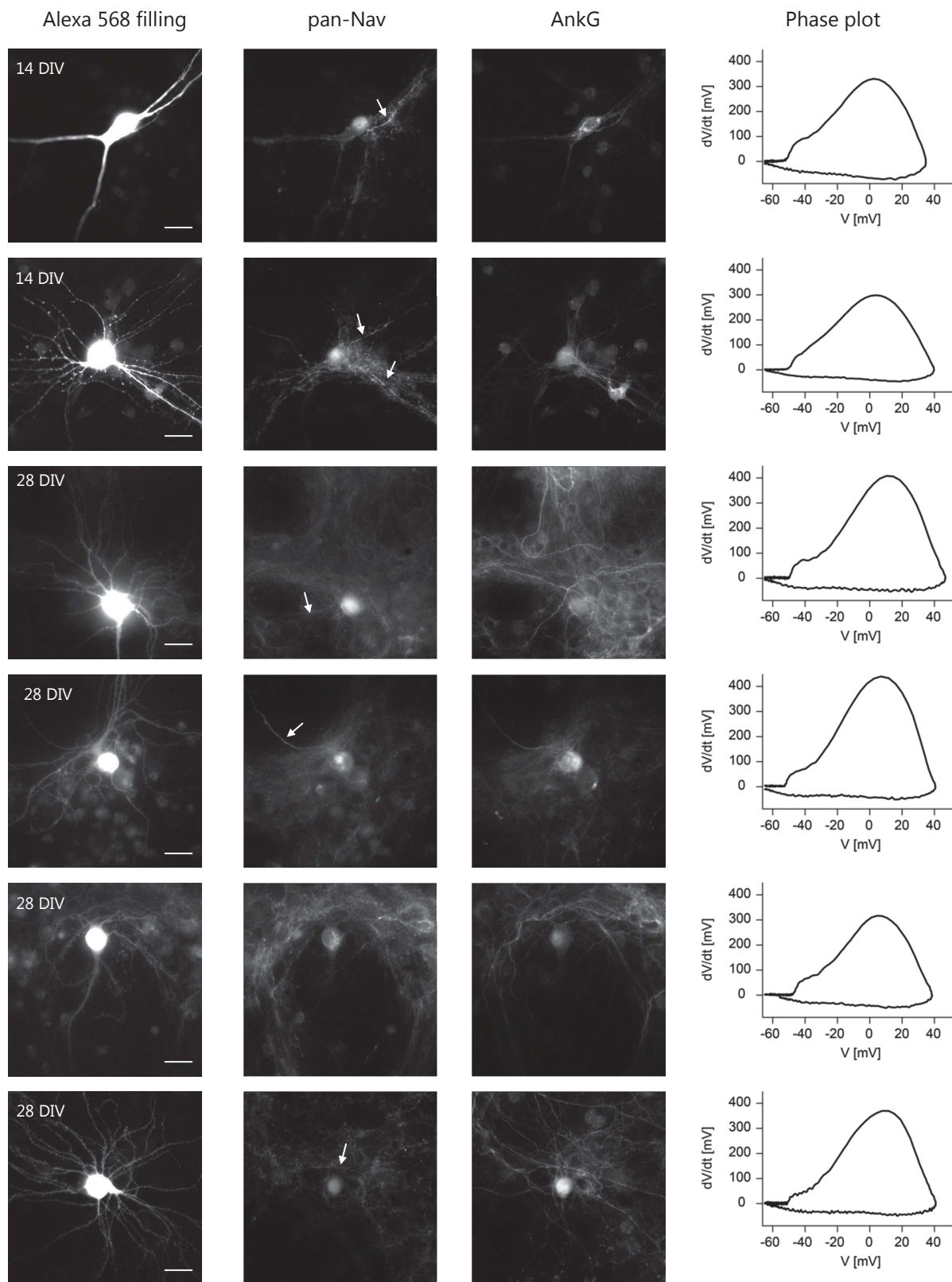


Figure S3 β IV-spectrin is absent in qv^{3J} mutants after first week of development, AnkG and pan-Nav are significantly reduced A Immunolabelling with two antibodies against non-mutated regions of β IV-spectrin (see methods) show reliable AIS labelling in all control but not qv^{3J} neurons. Scale bars are 20 μ m. The example images here are from DIV 26. B-C Detailed presentation of the immuno-fluorescence profiles for AnkG and pan-Nav from figure 3B & C). Here bootstrap 95% confidence intervals are shown for the mean fluorescence along the AIS, starting at the first branching point or the soma. D Example of a qv^{3J} neuron at DIV 7 stained for AnkG (C-terminal antibody) and β IV-spectrin (N-Terminal, OriGENE Antibody), demonstrating low levels of β IV-spectrin are still present in the AIS at this developmental stage, indicated by the weak yellow signal in the AIS.



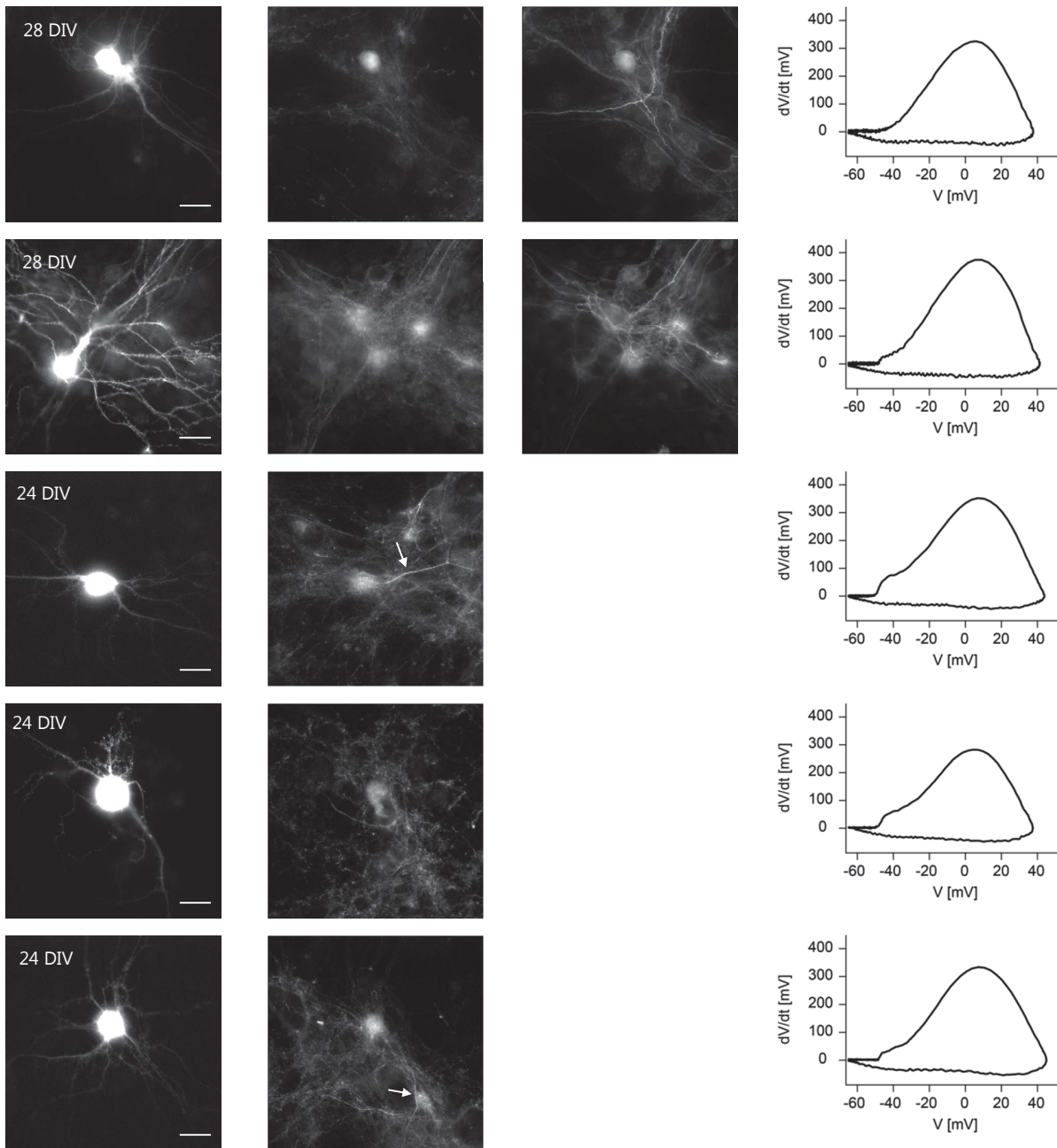


Figure S4: Immunolabeling and phase plane analysis of homozygous qv^{3J} mutant neurons at ages 14 - 28 DIV. The cells were filled with Alexa dye (left column) during whole-cell patch clamp recordings and were afterwards labeled with antibodies against pan-Nav channels and AnkG (excluding 3 cells) (second and third columns). White arrows mark the AIS in cases where we could potentially identify it based on matching Alexa staining and immunolabeling with AnkG. In some cases we were not able to determine its location. Phase plots of APs recorded from the cells are shown on the right column. Scale bar: 20 μ m. Note that each image of AnkG and pan-Nav labeling uses a different intensity scale (auto-scaled) and therefore their fluorescence intensities are not comparable.